Unconventional superparamagnetic behavior in the modified cubic spinel compound LiNi$_{0.5}$Mn$_{1.5}$O$_4$

S. S. Islam,[1] Vikram Singh ●,[1] K. Somesh,[1] Prashanta K. Mukharjee ●,[1] A. Jain,[2,3] S. M. Yusuf ●,[2,3] and R. Nath[1,*]

[1]*School of Physics, Indian Institute of Science Education and Research, Thiruvananthapuram-695551, India*
[2]*Solid State Physics Division, Bhabha Atomic Research Centre, Mumbai 400 085, India*
[3]*Homi Bhabha National Institute, Anushaktinagar, Mumbai 400 094, India*

Structural, electronic, and magnetic properties of modified cubic spinel compound LiNi$_{0.5}$Mn$_{1.5}$O$_4$ are studied via x-ray diffraction, resistivity, dc and ac magnetization, heat capacity, neutron diffraction, ^{7}Li nuclear magnetic resonance, magnetocaloric effect, magnetic relaxation, and magnetic memory effect experiments. We stabilized this compound in a cubic structure with space group $P4_332$. It exhibits semiconducting character with an electronic band gap of $\Delta/k_B \simeq 0.4$ eV. The interaction within each Mn^{4+} and Ni^{2+} sublattice and between Mn^{4+} and Ni^{2+} sublattices is found to be ferromagnetic (FM) and antiferromagnetic (AFM), respectively. This leads to the onset of a ferrimagnetic transition at $T_C \simeq 125$ K. The reduced values of frustration parameter (f) and ordered moments reflect magnetic frustration due to competing FM and AFM interactions. From the ^{7}Li nuclear magnetic resonance shift vs susceptibility plot, the average hyperfine coupling between ^{7}Li nuclei and Ni^{2+} and Mn^{4+} spins is calculated to be $\sim$672.4 Oe/μ_B. A detailed critical behavior study is done in the vicinity of T_C using modified-Arrott plot, Kouvel-Fisher plot, and universal scaling of magnetization isotherms. The magnetic phase transition is found to be second order in nature and the estimated critical exponents correspond to the three-dimensional XY universality class. A large magnetocaloric effect is observed with a maximum value of isothermal change in entropy $\Delta S_m \simeq -11.3$ J/Kg K and a maximum relative cooling power of RCP $\simeq 604$ J/Kg for 9 T magnetic field change. The imaginary part of the ac susceptibility depicts a strong frequency-dependent hump at $T = T_{f2}$ well below the blocking temperature $T_b \simeq 120$ K. The Arrhenius behavior of frequency dependent T_{f2} and the absence of zero-field-cooled memory confirm the existence of superparamagnetism in the ferrimagnetically ordered state.

I. INTRODUCTION

Geometrically frustrated quantum magnets have long been a field of attraction since they provide unique opportunity to realize novel quantum phases at low temperatures [1]. One of the most studied geometrically frustrated systems in three dimensions (3D) is the antiferromagnetic (AFM) pyrochlore lattice which features a network of corner-sharing tetrahedra. Prominent examples in this category are compounds with general formula AB_2O_4 (spinels), $A_2B_2O_7$ (pyrochlores), and AB_2. In particular, in spinel oxides AB_2O_4, B site ion forms a frustrated 3D pyrochlore lattice. Owing to ground-state degeneracy, these compounds have witnessed various exotic low-temperature phenomena ranging from quantum spin-liquid, spin-glass, field-induced transitions, magnetization plateaus to heavy fermionic behavior [2–4]. In addition, there exists another series of compounds AB_2X_6, often referred as cubic modified pyrochlore lattice which mostly contains either mixed-valent or two kinds of transition metal ions. The compounds (Rb,Cs)Cr$_2$F$_6$ [5], (K,Rb)Os$_2$O$_6$ [6], CsW$_2$O$_6$ [7], and CsNiCrF$_6$ [8] belong to this category and exhibit various exotic ground states.

Among the large class of spinel oxides, cubic LiMn$_2$O$_4$ (space group: $Fd\bar{3}m$, Mn^{3+} : Mn^{4+} = 1 : 1) is known to be a celebrated high-voltage cathode material for rechargeable Li-ion battery [9]. It is reported to have charge ordering accompanied by orbital ordering due to the Jahn-Teller distortion in Mn^{3+} ions and undergoes an antiferromagnetic (AFM) long-range ordering (LRO) at low temperatures [10]. In certain reports, the compound is found to show a spin-glass (SG) behavior without any magnetic LRO which is attributed to the Mn^{3+}/Mn^{4+} superlattice charge order as well as the effect of frustration [11]. These contradictory behaviors are believed to be originated from the Mn site disorder [12]. Recently, coexistence of LRO and SG state is found in LiMn$_2$O$_4$ nanorods [12]. The Ni-doped LiNi$_{0.5}$Mn$_{1.5}$O$_4$ (abbreviated as LNMO) crystallizes in two different phases depending on the synthesis conditions. The stoichiometric LNMO has $P4_332$ space group and exhibits a 1 : 3 cation order of Ni^{2+} and Mn^{4+} ions, while nonstoichiometric LiNi$_{0.5}$Mn$_{1.5}$O$_{4-\delta}$ has $Fd\bar{3}m$ space group [13].

In the $Fd\bar{3}m$ structure, Ni and Mn atoms randomly occupy one crystallographic site while in the $P4_332$ structure, they occupy two inequivalent sites independently. In the $P4_332$ structure which can also be referred as modified cubic spinel, the edge sharing of MnO$_6$ and NiO$_6$ octahedra and the corner-shared LiO$_4$ tetrahedra lead to a complex three-dimensional (3D) structure [see Fig. 1(a)]. When only the interaction among the Mn^{4+} ions is considered, LNMO forms a 3D network of corner-sharing Mn^{4+} triangles which is found to be a frustrated hyperkagome lattice [see Fig. 1(b)]. Further, when the interaction between Mn^{4+} and Ni^{2+} ions is taken
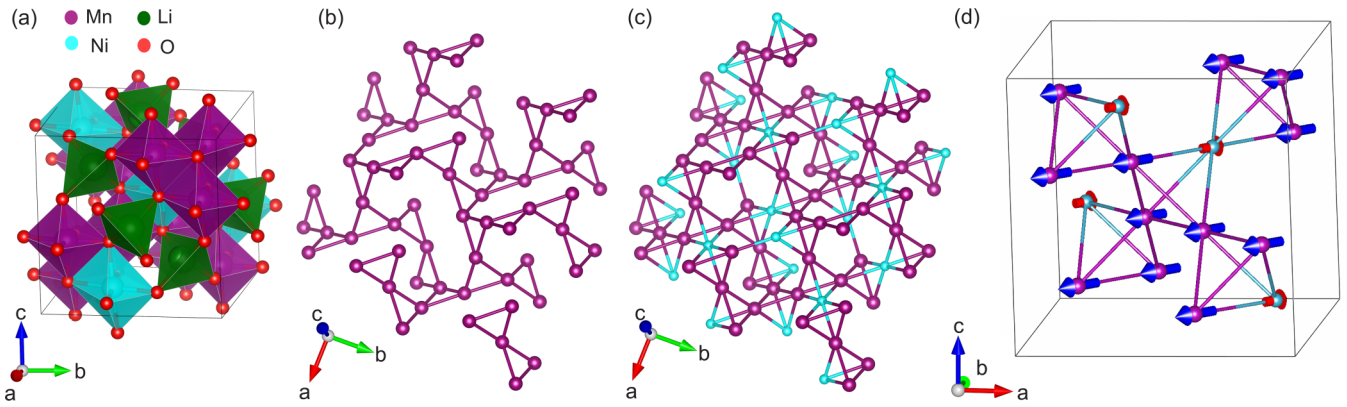
FIG. 1. (a) Crystal structure of LNMO in three dimensions. (b) Hyperkagome lattice made of Mn^{4+} ions. (c) Pyrochlore lattice made of Ni^{2+} and Mn^{4+} ions. (d) A section of the pyrochlore lattice showing corner-sharing tetrahedra and spin structure deduced from the neutron diffraction data at $T = 5$ K.

into account, a network of corner-shared tetrahedra is formed where each tetrahedron consists of three Mn^{4+} and one Ni^{2+} ions. Hence, the hyperkagome lattice transforms into a 3D pyrochlore lattice [see Fig. 1(c)]. Based on the preliminary magnetic measurements, LNMO is reported to show a magnetic transition at $T_C \simeq 125$ K [14].

In this paper, we present a detailed study of the physical properties of stoichiometric modified cubic spinel compound LNMO ($P4_332$). A ferrimagnetic order is detected at $T_C \simeq 125$ K. We found that the interaction within each Mn^{4+} and Ni^{2+} sublattice is ferromagnetic (FM), whereas the interaction between these two sublattices is antiferromagnetic (AFM), which results in a ferrimagnetic behavior below T_C. Multiple magnetic transitions are observed below T_C, likely due to magnetic frustration. It exhibits magnetic relaxation and magnetic memory effect below T_C, typically expected for superparamagnetic systems. A large magnetocaloric effect (MCE) is obtained across the magnetic transition. The critical analysis of magnetization and MCE data establish LNMO as a 3D XY-type magnet. The paper is organized in the following manner. The experimental details concerning sample preparation and various measurements are described in Sec. II. Section III contains the experimental results which includes powder x-ray diffraction, resistivity, dc magnetization, heat capacity, neutron diffraction, ^{7}Li nuclear magnetic resonance (NMR), magnetocaloric effect, ac susceptibility, magnetic relaxation, and magnetic memory effect measurements, followed by discussions. Our experimental findings are summarized in Sec. IV.

II. METHODS

Traditional sol-gel synthesis method was adopted to synthesize LNMO in polycrystalline form. At first, stoichiometric amount of lithium nitrate (LiNO$_3$, 99.99%), manganese nitrate tetrahydrate [Mn(NO$_3$)$_2$.4H$_2$O, $\geqslant$97%], and nickel nitrate hexahydrate [Ni(NO$_3$)$_2$.6H$_2$O, 99.999%] were taken and dissolved into ethanol. The mixture was continuously stirred at 80 °C until the whole solvent is evaporated from the mixture and dark black colored paste was found. The resulting paste was then transferred into a crucible and preheated at 500 °C for 2 h and then at 800 °C for 8 h. Subsequently, the furnace

was switched off and the sample was cooled naturally within the furnace. The resultant sample was found to be formed in the space group $Fd\bar{3}m$, confirmed from the powder x-ray diffraction. In the next step, the resultant sample was ground thoroughly and pressed into pellets. The pellets were heated at 700 °C for 2 days and then cooled very slowly to room temperature at a rate of 0.1 °C/min. This post firing of the $Fd\bar{3}m$ phase sample at 700 °C was done to ensure the formation of the cation ordered $P4_332$ phase. This method is well established and already experimented previously [15].

Phase purity of the sample was checked from the high-quality powder x-ray diffraction (XRD) data, collected using a PANalytical x-ray diffractometer (Cu K_α radiation, $\lambda_{av} \simeq$ 1.5418 Å). The temperature-dependent powder x-ray diffraction was performed over a wide temperature range (15 K $\leqslant$ $T \leqslant$ 300 K). For going below room temperature, an Oxford Phenix low-temperature attachment to the diffractometer was used. To solve the magnetic structure, temperature-dependent neutron powder diffraction (NPD) experiment was performed using the neutron powder diffractometer PD-I ($\lambda \simeq$ 1.094 Å) with three linear position-sensitive detectors at Dhruva reactor, Bhabha Atomic Research Center, India. Rietveld refinement of the powder XRD data and NPD data was performed using FULLPROF software package [16].

The dc magnetization (M) was measured using a vibrating sample magnetometer (VSM) attachment to a commercial Physical Property Measurement System (PPMS, Quantum Design) as a function of temperature (2 K $\leqslant$ $T \leqslant$ 600 K) and magnetic field (0 to 9 T). For the high-temperature measurements ($T \geqslant$ 380 K), a high-T oven was attached to the VSM. Similarly, ac susceptibility was measured as a function of temperature (2 K $\leqslant$ $T \leqslant$ 200 K) and frequency (50 Hz $\leqslant$ $\nu \leqslant$ 10 kHz) in an ac field of 5 Oe using ACMS option of the PPMS. For the temperature-dependent heat capacity (C_p) measurement, the relaxation technique was adopted and the measurement was carried out on a pressed pellet using heat-capacity option of the PPMS. Electrical resistivity (ρ) as a function of temperature was measured on a rectangular pellet using the four-probe technique in PPMS.

The NMR measurements were performed by employing pulsed NMR technique on ^{7}Li (nuclear spin $I = \frac{3}{2}$ and gyromagnetic ratio $\gamma_N/2\pi = 16.546$ MHz/T) nuclei over a wide
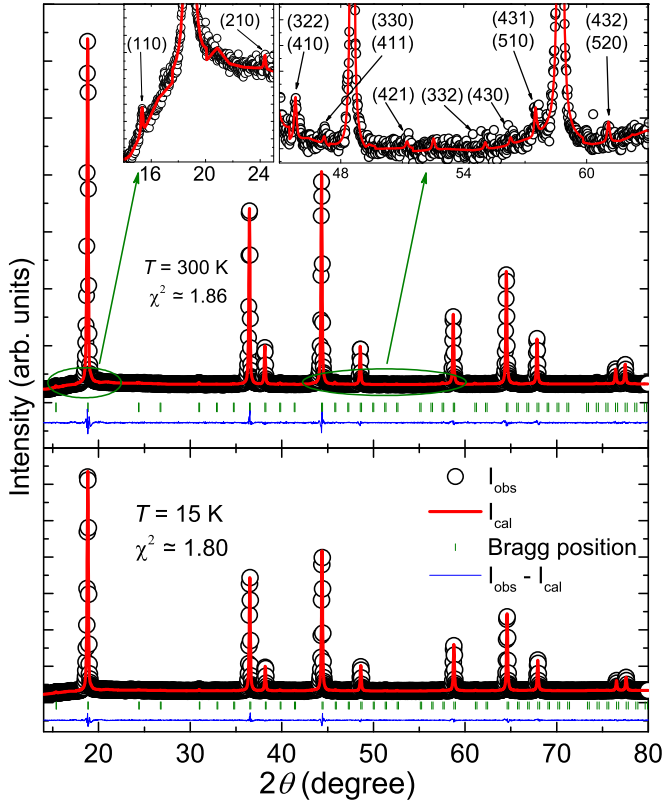
FIG. 2. Upper panel: x-ray powder diffraction pattern (open circles) of LNMO at room temperature. The red solid line is the Rietveld refinement fit with $P4_332$ space group. The expected Bragg positions are indicated by green vertical ticks. Blue solid line at the bottom denotes the difference between observed and calculated intensities. Inset: enlarged portion of the XRD pattern to visualize small Bragg peaks. Lower panel: Rietveld refinement of the XRD pattern of LNMO at 15 K.

temperature range (4 K $\leqslant T \leqslant$ 290 K). For this purpose, we have used a liquid-helium cryostat (Janis, USA) with a field sweep superconducting magnet and a Tecmag (Redstone) spectrometer. The spectral measurements at different temperatures were carried out either by Fourier transform of the NMR echo signal at a fixed field of $H = 1.5462$ T or by sweeping the field at a corresponding fixed frequency of 25.58 MHz. Traditional saturation recovery pulse sequence was used to measure the ^{7}Li spin-lattice relaxation time (T_1).

III. RESULTS AND DISCUSSION

A. X-ray Diffraction

Figure 2 presents the XRD pattern of LNMO at two end temperatures 300 and 15 K. To evaluate the unit cell parameters and atomic positions, Rietveld refinement was performed on the powder XRD data. The initial structural parameters for this purpose were taken from Ref. [15]. All the peaks could be successfully indexed with cubic noncentrosymmetric space group $P4_332$. The refined unit cell parameters, volume of the unit cell, and the atomic coordinates at room temperature are listed in Table I which are in close agreement with the previous paper. As already described in Sec. I, LNMO exhibits

TABLE I. Crystal structure data for LNMO at room temperature (cubic, space group: $P4_332$). The obtained lattice parameters from the refinement are $a = b = c = 8.1643(1)$ Å and $V_{cell} \simeq 544.2$ Å^3. Our fit yields quality factors $R_p \simeq 10.1$, $R_{wp} \simeq 6.66$, $R_e \simeq 4.88$, and goodness of fit $\chi^2 = [\frac{R_{wp}}{R_e}]^2 \simeq 1.87$. Listed are the Wyckoff positions and the refined atomic coordinates (x, y, and z) for each atom.

Atom	Site	x	y	z
Li	$8c$	$-0.0002\,(4)$	$-0.0002\,(4)$	$-0.0002\,(4)$
Ni	$4b$	0.625	0.625	0.625
Mn	$12d$	0.125	0.3768 (3)	0.8732 (3)
O1	$8c$	0.3816 (7)	0.3816 (7)	0.3816 (7)
O2	$24e$	0.1509 (6)	-0.1395 (9)	0.1238 (7)

1:3 cation order, resulting in a superstructure cubic $P4_332$ space group. The cation ordering in LNMO can be visualized by the emergence of several low angle and low intensity Bragg peaks, such as (110), (210), (322), (410), etc. [17]. These peaks are not allowed in the Bragg reflections in the normal face-centered-cubic spinel ($Fd\bar{3}m$) structure because of the reflection conditions $(h + k) = 2n$, $(h + l) = 2n$, and $(k + l) = 2n$. Here, n is the integer and (h, k, l) are the Miller indices. These low-intensity peaks are highlighted in the inset of the upper panel of Fig. 2. It can be seen that all these small Bragg reflections could be perfectly indexed by using $P4_332$ space group. We have also tried to do the refinement with $Fd\bar{3}m$ space group, which could not index these small Bragg peaks, thus confirming the phase purity of the sample with $P4_332$ space group.

It is reported that the material synthesis following sol-gel method leads to the formation of nanocrystalline form of LNMO [18]. To estimate the crystallite size, we fitted the XRD peaks at room temperature by a Gaussian function and evaluated the full width at half-maxima (FWHM) of the individual peak. Subsequently, by using the Scherrer equation $\tau = K\lambda/\beta\cos\theta$ (where τ is the crystallite size, K is the dimensionless shape factor which has a typical value of 0.9, λ is the x-ray wavelength, and β is the line broadening at FWHM), the average crystallite size is calculated to be $\sim$60 nm [19]. Further, the analysis of the scanning-electron-microscopy (SEM) data also reveals the nanocrystalline nature of LNMO sample with average particle size 100–150 nm.

As shown in lower panel of Fig. 2, no extra peaks could be detected down to 15 K. Figure 3 depicts the temperature variation of lattice constant (a) and unit cell volume [$V_{cell}(T)$] obtained from the refinement. Both the quantities are found to decrease systematically during cooling and neither any structural transition nor any lattice distortion is observed in the entire measured temperature range (15 K $\leqslant T \leqslant$ 300 K). Following the method described in Ref. [20], $V_{cell}(T)$ is fitted by

$$V_{cell}(T) = \gamma U(T)/K_0 + V_0, \qquad (1)$$

where V_0 is the unit cell volume of the crystal structure at $T = 0$ K, K_0 is the bulk modulus, and γ is the Grüneisen parameter. $U(T)$ is the internal energy and it can be expressed in terms
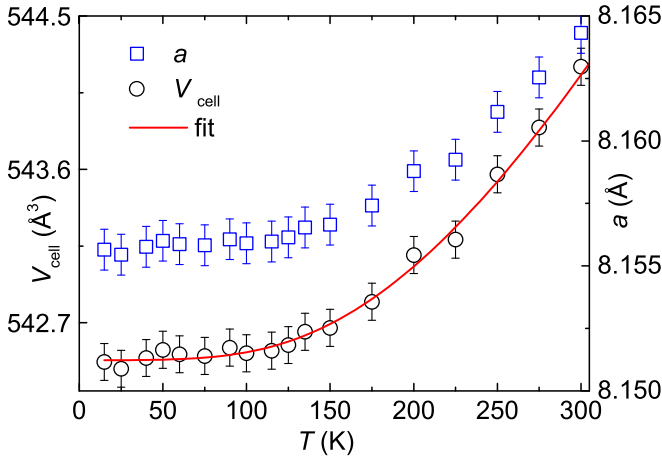
FIG. 3. Variation of lattice constant (*a*) and unit cell volume (V_{cell}) with temperature. The solid line represents the fit of $V_{cell}(T)$ by Eq. (1).

of the Debye approximation as

$$U(T) = 9p\,k_B T \left(\frac{T}{\theta_D}\right)^3 \int_0^{\theta_D/T} \frac{x^3}{e^x - 1} dx. \qquad (2)$$

Here, *p* is the number of atoms in the unit cell and k_B is the Boltzmann constant. The parameters evaluated from the fitting are Debye temperature $\theta_D \simeq 965$ K, $\gamma/K_0 \simeq 1.24 \times 10^{-4}$ Pa^{-1}, and $V_0 \simeq 542.48$ Å^3.

B. Resistivity

Temperature-dependent electrical resistivity [$\rho(T)$] measured in zero field is shown in Fig. 4. It increases rapidly with decreasing temperature which indicates that the ground state is insulating in nature. Below 218 K, $\rho(T)$ could not be measured since it exceeded the measurable range of the instrument. To evaluate the activation energy, the temperature-dependent conductivity ($\sigma = 1/\rho$) data were
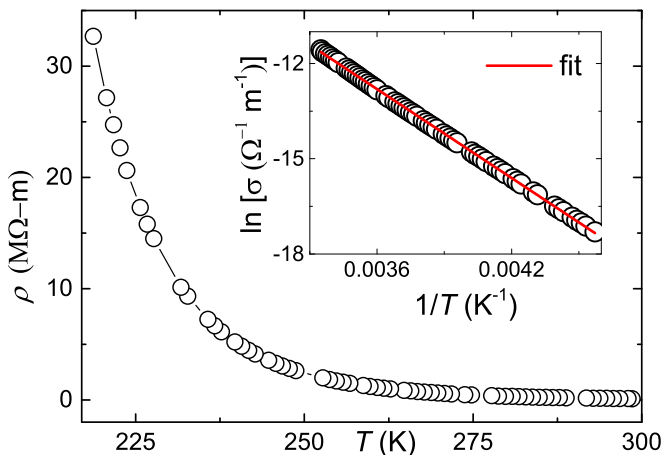

FIG. 4. The electrical resistivity $\rho(T)$ of LNMO in zero field. Inset: ln(σ) vs $1/T$. The solid line is the fit using Eq. (3).
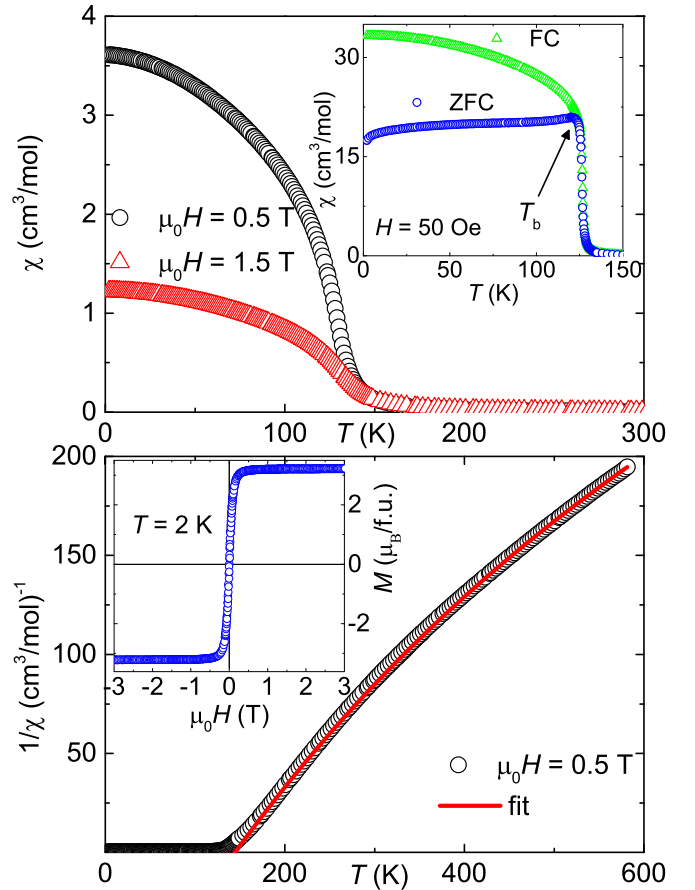

FIG. 5. Upper panel: temperature-dependent dc magnetic susceptibility $\chi(T)$ at two different applied fields. Inset: $\chi(T)$ measured at 50 Oe in ZFC and FC conditions. Lower panel: $1/\chi$ vs T in $\mu_0 H = 0.5$ T. Inset: magnetization isotherm at $T = 2$ K.

fitted by Arrhenius equation

$$\sigma(T) = A \exp\left(-\frac{\Delta}{k_B T}\right), \qquad (3)$$

where *A* is the proportionality constant and Δ is the activation energy. In the inset of Fig. 4, ln(σ) is plotted against $1/T$ to highlight the activated behavior. Our fit in the whole measured temperature range (218 K $\leqslant T \leqslant$ 300 K) yields $\Delta/k_B \approx 0.4$ eV. This value of Δ/k_B categorizes LNMO as a semiconductor.

C. dc magnetization

The upper panel of Fig. 5 presents the temperature-dependent dc magnetic susceptibility $\chi(T)$ ($\equiv M/H$) measured in an applied field of $\mu_0 H = 0.5$ and 1.5 T. In the high-temperature regime, $\chi(T)$ shows a gradual increase with decreasing temperature. Below about 140 K, $\chi(T)$ increases rapidly, indicating the onset of a ferrimagnetic/ferromagnetic ordering. From the $d\chi/dT$ vs T plot, the ordering temperature is found to be $T_C \simeq 125$ K. As depicted in the inset of the upper panel of Fig. 5, the zero-field-cooled (ZFC) and field-cooled (FC) susceptibility data at $H = 50$ Oe show a significant bifurcation below T_C. Such an irreversibility is a characteristic behavior of ferrimagnetic/ferromagnetic

compounds [21] and is also observed for various SG [22,23] and superparamagnetic [24] systems. Moreover, the ZFC $\chi(T)$ shows a well defined maxima at $T_b \simeq 120$ K, which corresponds to the blocking temperature, typically expected for a superparamagnet. A significant difference in the behavior of FC $\chi(T)$ is expected between a superparamagnet and a SG system. For instance, FC magnetization always increases for a superparamagnet whereas for a SG system, it either remains flat or decreases with decreasing temperature, below T_b [25,26]. As noticed from Fig. 5, the FC $\chi(T)$ below T_b increases monotonously with decreasing T, which is a primary indication of the superparamagnetic blocking process [25,27]. In order to confirm this behavior, we have performed a detailed ac susceptibility and magnetic memory effect experiments which are discussed later.

The lower panel of Fig. 5 shows the inverse magnetic susceptibility $(1/\chi)$ for $\mu_0 H = 0.5$ T. In the paramagnetic regime $(T > T_C)$, $1/\chi$ typically shows a linear behavior with temperature, due to uncorrelated moments. In contrast, the observed high-temperature nonlinear behavior with a strong positive curvature is a possible signature of ferrimagnetic nature of LNMO [21,28]. To extract the magnetic parameters, we fitted the $\chi(T)$ data by the modified Curie-Weiss law

$$\chi(T) = \chi_0 + \frac{C}{T - \theta_{CW}}. \qquad (4)$$

Here, χ_0 is the temperature-independent susceptibility, C is the Curie constant, and θ_{CW} is Curie-Weiss temperature. Our fit in the high-temperature regime $(T \geqslant 450$ K) (see the lower panel of Fig. 5) yields the parameters $\chi_0 \simeq 0.0015$ cm^3/mol, $C \simeq 1.604$ cm^{3}K/mol, and $\theta_{CW} \simeq 144.4$ K. From the value of C, the effective moment is calculated to be $\mu_{eff} = \sqrt{3k_B C/N_A \mu_B^2} \simeq 3.58\mu_B$, where N_A is the Avogadro's number. This is close to the expected spin only value of

$$\mu_{eff} = \sqrt{\left(\frac{0.5 \times [\mu_{eff}(Ni^{2+})]^2 + 1.5 \times [\mu_{eff}(Mn^{4+})]^2}{0.5 + 1.5} \right)} \mu_B =$$

$3.64\mu_B$, taking $\mu_{eff} = 2.83\mu_B$ and $3.87\mu_B$ for Ni$^{2+}(S = 1)$ and Mn$^{4+}(S = \frac{3}{2})$, respectively [14]. The positive value of θ_{CW} implies that the dominant interaction among the magnetic ions is ferromagnetic (FM) in nature. The inset of the lower panel of Fig. 5 shows a complete magnetization isotherm (M vs H) at $T = 2$ K. It shows a very weak hysteresis and the magnetization saturates quickly at $\mu_0 H = 0.5$ T, typically expected for a ferrimagnet. The saturation magnetization (M_s) is found to be $\sim 3.2\mu_B$. Assuming a two-sublattice model of magnetic species Ni^{2+} and Mn^{4+} with antiferromagnetic (AFM) coupling between them and using molecular-field approximation, the saturation magnetization for LNMO can be written as $M_s = [S(Mn^{4+}) \times g \times 1.5 - S(Ni^{2+}) \times g \times 0.5]\mu_B$ [21,28]. Taking $S(Mn^{4+}) = \frac{3}{2}$, $S(Ni^{2+}) = 1$, and $g = 2$, M_s is calculated to be $3.5\mu_B$. Usually, the value of g for Mn^{4+} and Ni^{2+} is always more than 2 which should produce M_s larger than $3.5\mu_B$ [29]. Clearly, our experimental value of M_s is smaller than the expected spin only value.

The extent of frustration in a spin system can be quantified by the frustration ratio $f = \frac{|\theta_{CW}|}{T_C}$ [1]. According to the mean field theory, θ_{CW} is nothing but the sum of all exchange cou-
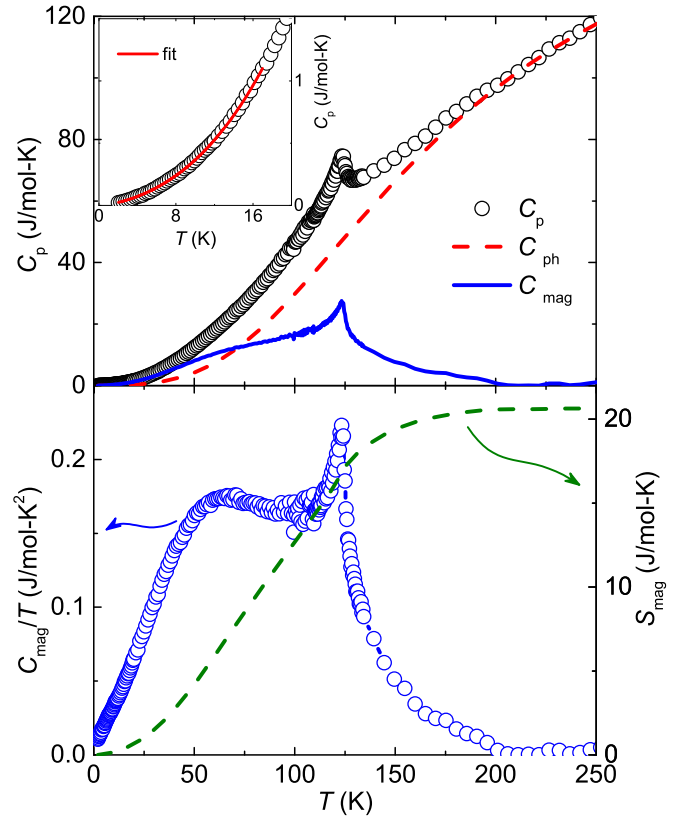

FIG. 6. Upper panel: $C_p(T)$ measured in zero magnetic field. The dashed and solid lines represent the phonon (C_{ph}) and magnetic (C_{mag}) contributions, respectively. Inset: enlarged view of low-temperature portion of $C_p(T)$ data. The solid line is the fit as described in text. Lower panel: C_{mag}/T and magnetic entropy (S_{mag}) vs T along the left and right y-axes, respectively.

plings present in the system i.e., $\theta_{CW} = \sum_i J_i$, where i is the number of nearest-neighbor spins [30]. Typically, for a non-frustrated AFM system $\theta_{CW} \sim T_C$ (or T_N) and f has a value close to 1. However, for a highly frustrated antiferromagnet, f value is much larger than 1 (>10) [31]. On the other hand, for a system having FM and AFM interactions, the value of θ_{CW} is reduced due to opposite sign of the exchange couplings. This results in a decreased value of f. For LNMO, the frustration ratio is calculated to be $f \simeq 144.4/125 \simeq 1.16$. Since LNMO is having highly frustrated pyrochlore geometry, a reduced value of f clearly implies coexistence of AFM and FM interactions in the system. Indeed, our neutron powder diffraction experiments (discussed later) confirm this proposition.

D. Heat capacity

The temperature-dependent heat capacity [$C_p(T)$] measured in zero field is shown in the upper panel of Fig. 6. A sharp and distinct peak is observed at $T_C \simeq 124$ K, indicating the magnetic transition. In order to analyze the low-temperature $C_p(T)$ data, we first used the relation $C_p(T) = \beta T^3$, which did not fit the data effectively. However, the low-temperature $C_p(T)$ data could be fitted nicely by adding an extra term $\delta T^{3/2}$ to the above relation i.e., $C_p(T) = \beta T^3 + \delta T^{3/2}$. Here, the first term ($\beta T^3$) represents
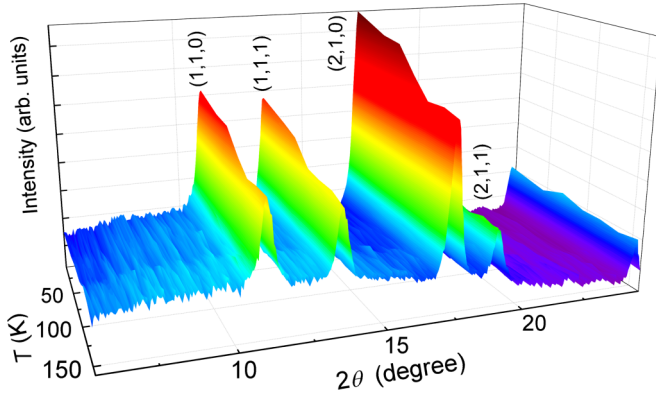
FIG. 7. Temperature evolution of the neutron powder diffraction pattern of LNMO shown for the low-angle regime. An enhancement in the intensity of fundamental nuclear Bragg peaks is evident below T_C. These Bragg peaks at $2\theta \simeq 10.81°$, $13.31°$, $17.17°$, and $18.84°$ correspond to $(1,1,0)$, $(1,1,1)$, $(2,1,0)$, and $(2,1,1)$ planes, respectively.

the lattice contribution and the second term ($\delta T^{3/2}$) is typical for ferromagnetic/ferrimagnetic and glassy systems [32,33]. The inset of the upper panel of Fig. 6 depicts the enlarged view of the low-temperature portion of $C_p(T)$. The solid line is the fit using the above relation, in the temperature range 2–16 K. The resulting β and δ values are $\sim 1.07 \times 10^{-4}$ J mol^{-1} K^{-4} and ~ 0.0081 J mol^{-1} K$^{-5/2}$, respectively. The electronic contribution γT is not considered in the fitting procedure since LNMO is an insulator at low temperatures.

For an estimation of the phonon contribution $C_{ph}(T)$, we fitted the experimental $C_p(T)$ data in the high-temperature regime ($T \geqslant 160$ K) by the Debye function

$$C_{ph}(T) = 9R\left(\frac{T}{\theta_D}\right)^3 \int_0^{\theta_D/T} \frac{x^4 e^x}{(e^x - 1)^2} dx. \qquad (5)$$

Here, R is the universal gas constant. The best fit was obtained with $\theta_D \simeq 735$ K which is close to the value obtained from the $V_{cell}(T)$ analysis. The high-temperature $C_{ph}(T)$ fit was extrapolated down to low temperatures and subtracted from the experimental $C_p(T)$ data to obtain the magnetic contribution $C_{mag}(T)$. The obtained $C_{mag}(T)$ is shown as a solid line in the upper panel of Fig. 6. $C_{mag}(T)/T$ vs T is presented in the left y-axis of the lower panel of Fig. 6. The magnetic entropy $S_{mag}(T)$ is calculated by integrating the $C_{mag}(T)/T$ in the whole measured temperature range as

$$S_{mag}(T) = \int_{2.1\,K}^T \frac{C_{mag}(T)}{T} dT. \qquad (6)$$

As shown in the lower panel of Fig. 6, the value of S_{mag} is found to be ~ 20.6 J/mol K at 250 K, which is very close to the theoretically expected value of $S_{mag} = 0.5 \times R \ln[2S(Ni^{2+}) + 1] + 1.5 \times R \ln[2S(Mn^{4+}) + 1] = 21.8$ J/mol K. One broad hump is observed in $C_{mag}(T)$ at around $T \sim 50$ K which cannot be attributed to any magnetic transition as $\chi(T)$ does not show any feature at this temperature. Similar feature is reported earlier for BaMn$_2$As$_2$ and BiMn$_2$PO$_6$ where it is proposed that this broad hump is associated with the temperature dependent change in the population of the Zeeman levels
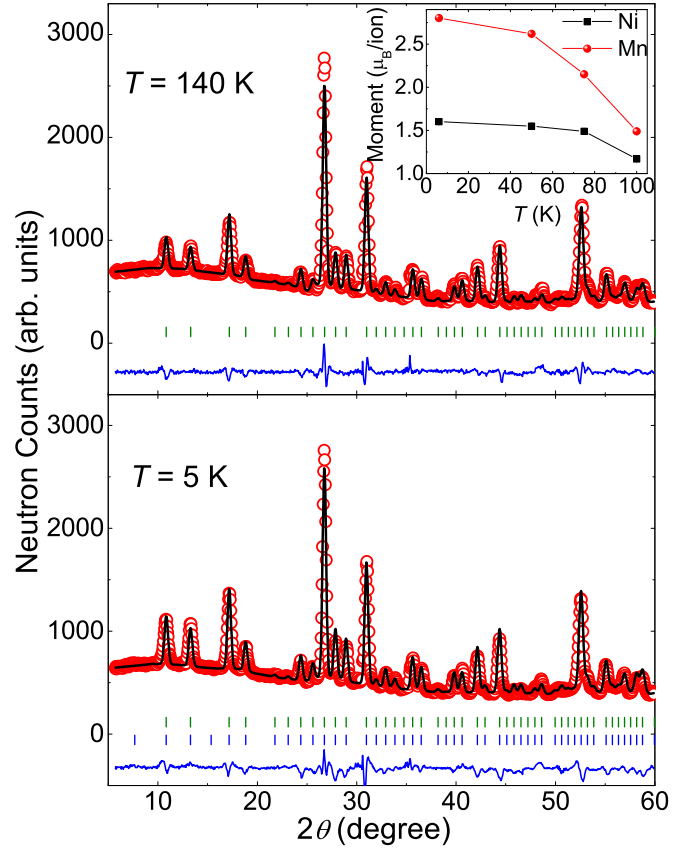

FIG. 8. Rietveld refined neutron powder diffraction patterns at $T = 140$ K (upper panel) and $T = 5$ K (lower panel). Open circles represent the experimental data, solid line represents the calculated curve, and difference between them is shown as a solid line at the bottom. Vertical marks correspond to the position of all allowed Bragg reflections for the nuclear (top row) and magnetic (bottom row) reflections. Inset: temperature variation of ordered magnetic moment for Ni^{2+} and Mn^{4+} ions.

below transition, arising due to the temperature dependent exchange field [34,35]. Using a Weiss molecular field theory on a Heisenberg model, it is predicted that the humplike feature is pronounced for the systems with higher spin values [34,35]. Thus, the observed hump in $C_{mag}(T)$ is obvious since LNMO has two high spins: $S = 1$ and $S = \frac{3}{2}$.

E. Neutron diffraction

Figure 7 depicts a series of neutron powder diffraction (NPD) patterns for LNMO, over the temperature range 5–300 K. An enhancement in the intensity of fundamental nuclear Bragg peaks at $\sim 10.81°$, $13.31°$, $17.17°$, and $18.84°$ are observed below T_C. The observation of additional intensity at the positions of fundamental nuclear Bragg reflections (with no additional peaks) indicate the presence of a ferromagnetic or ferrimagnetic ordering. As shown in the upper panel of Fig. 8, all the nuclear peaks at $T = 140$ K could be refined using cubic crystal structure with space group $P4_332$. The refined structural parameters are listed in Table II. These values are in close agreement with the refined values obtained from the powder XRD data. The lower panel of Fig. 8 shows the

TABLE II. Structural parameters of LNMO refined from the neutron diffraction data at $T = 140$ K (structure: cubic and space group: $P4_332$). The obtained lattice parameters from the refinement are $a = b = c = 8.2000(8)$ Å and $V_{cell} \simeq 551.36(9)$ Å^3. The fit yields quality factors $R_p \simeq 21.5$, $R_{wp} \simeq 18.2$, $R_e \simeq 15.8$, and goodness of fit $\chi^2 = [\frac{R_{wp}}{R_e}]^2 \simeq 1.327$. Listed are the Wyckoff positions and the refined atomic coordinates (x, y, and z) for each atom.

Atom	Site	x	y	z
Li	8c	0.0002(19)	0.0002(19)	0.0002(19)
Ni	4b	0.625	0.625	0.625
Mn	12d	0.125	0.3787(11)	0.8713(11)
O1	8c	0.3809(5)	0.3809(5)	0.3809(5)
O2	24e	0.1503(4)	−0.1417(5)	0.1298(5)

Rietveld refinement of NPD pattern at $T = 5$ K. All the low-angle peaks with additional intensity could be indexed with a propagation vector $k = (0, 0, 0)$ and space group $P4_332$. The symmetry analysis shows that the observed NPD patterns can be fitted assuming a collinear ferrimagnetic structure with magnetic moments aligned along the [110] direction. The magnetic spin structure determined from Rietveld refinement of the NPD pattern at $T = 5$ K is shown in Fig. 1(d). Within each Ni^{2+} or Mn^{4+} sublattice, the moments are arranged parallel to each other providing a FM intrasublattice interaction whereas between the Ni^{2+} and Mn^{4+} sublattices the alignment is found to be antiparallel, which provides an AFM intersublattice interaction. From Fig. 1(d) it is clearly evident that the system is still frustrated due to competing FM and AFM interactions. However, the extent of frustration is definitely less than a conventional AFM pyrochlore lattice. This indeed falls in line with the $\chi(T)$ analysis where the reduced value of f is attributed to the coexistence of AFM and FM interactions.

One can also understand the exchange interactions by looking at the bond angles. From the refinement of NPD data at $T = 5$ K, we found the angles $\angle$Mn-O1-Mn $\simeq 93.8°$, $\angle$Mn-O2-Mn $\simeq 98.4°$, and $\angle$Mn-O2-Ni $\simeq 96.80°$ and 95.3°. According to Goodenough-Kanamori rule [36], the superexchange interaction between Mn^{4+} ($3d^3$) ions through the O^{2-} ($2p^2$) ion is expected to be AFM when the angle $\angle$Mn-O-Mn is linear ($\sim 180°$) and it crosses over to FM interaction for the angle $<135°$ [37]. On the contrary, for the interaction between Mn^{4+} ($3d^3$) and Ni^{2+} ($3d^8$) ions via O^{2-} ($2p^2$) ion, it is reported that FM interaction occurs for angle $\angle$Mn-O-Ni close to 180° and AFM interaction for the angle close to 90° [36]. Thus, the obtained FM interaction between Mn^{4+} ions and AFM interaction between Mn^{4+} and Ni^{2+} ions is consistent with the bond angle analysis using NPD data.

At $T = 5$ K, the refined values of the ordered moment at 4b (Ni^{2+}) and 12d (Mn^{4+}) sites are found to be $\mu = 1.60(1)\mu_B$ and $2.80(1)\mu_B$, respectively, which are smaller as compared to the expected spin-only values ($2\mu_B$/Ni^{2+} for $S = 1$ and $3\mu_B$/Mn^{4+} for $S = \frac{3}{2}$), assuming $g = 2$. Such a reduced moment is typically observed in low-dimensional and frustrated spin systems which is attributed to the effect of quantum fluctuations and magnetic frustration, respectively [38]. As shown in the inset of Fig. 8 the value of the ordered moment for both Ni^{2+} and Mn^{4+} decreases as the temperature
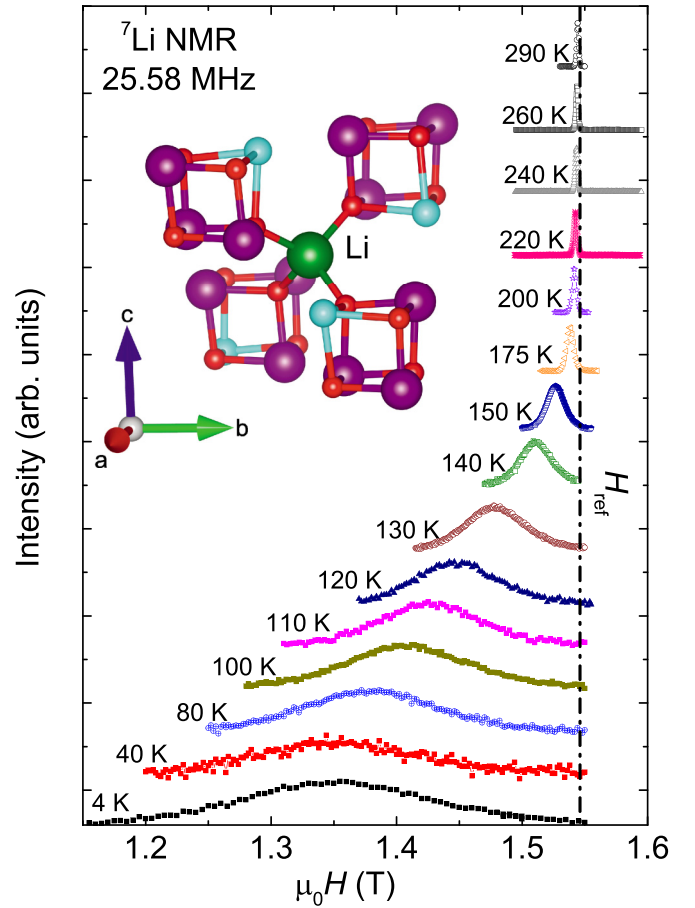

FIG. 9. Field-sweep ^{7}Li NMR spectra at different temperatures for the polycrystalline LNMO sample measured at 25.58 MHz. The vertical dashed line corresponds to the ^{7}Li resonance frequency of the nonmagnetic reference. Inset: coupling of Li nucleus with four cubic units made of Ni^{2+} and Mn^{4+} ions.

approaches T_C, typical behavior of sublattice magnetization in the ordered state. Using these values of the ordered moments at $T = 5$ K, one expects a saturation magnetization of $M_s \simeq (\mu_{Mn^{4+}} \times 1.5 - \mu_{Ni^{2+}} \times 0.5)\mu_B \simeq 3.4\mu_B$, assuming a ferrimagnetic spin structure which is indeed consistent with $M_s \simeq 3.2\mu_B$ obtained from the M vs H curve at $T = 2$ K.

F. ^{7}Li NMR

Since Li is coupled strongly with the magnetic Mn^{4+} and Ni^{2+} ions (see the inset of Fig. 9) it is possible to get the information about the static and dynamic properties of the spins by performing ^{7}Li NMR.

1. ^{7}Li NMR spectra

For a quadrupolar ^{7}Li ($I = \frac{3}{2}$) nucleus, one would expect two satellite peaks along with the central line due to three allowed transitions. Our ^{7}Li NMR spectra, however, display a single spectral line in the whole temperature range as shown in Fig. 9 which corresponds to the central transition ($+\frac{1}{2} \leftrightarrow -\frac{1}{2}$). The absence of satellite peaks could be either due to low quadrupolar frequency or the distribution of the satellite peak intensity over a wide frequency/field range. A single spectral
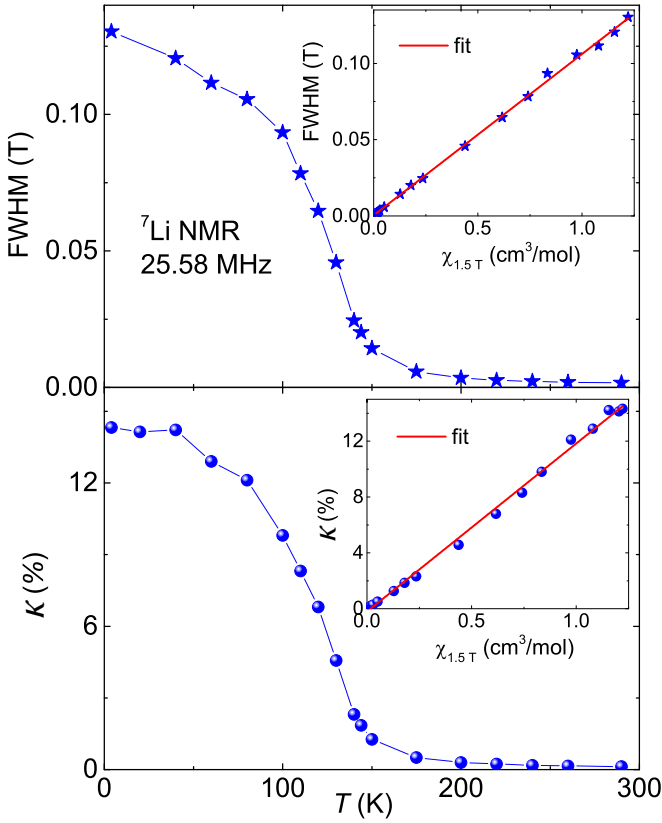
FIG. 10. Upper panel: full width at half-maximum (FWHM) of ^{7}Li NMR spectra plotted as a function temperature. Inset: FWHM vs χ measured at 1.5 T is plotted with temperature as an implicit parameter. The solid line is a linear fit. Lower panel: temperature-dependent ^{7}Li NMR shift (K) vs temperature. Inset: ^{7}Li NMR shift vs χ measured at 1.5 T is plotted with temperature as an implicit parameter. The solid line is a linear fit.

line in ^{7}Li NMR is typically observed in low-dimensional oxides [39]. The line shape is found to be symmetric in the entire measured temperature range suggesting the absence of magnetic anisotropy in the compound. The NMR line broadens drastically below T_C which reflects that Li nucleus senses the static internal field in the ordered state. With decreasing temperature, the peak position of the spectral line is found to be shifted. The upper panel of Fig. 10 depicts the full width at half-maximum (FWHM) of ^{7}Li NMR spectra plotted as a function temperature. At high temperatures ($T \geqslant 200$ K), it is almost temperature independent, increases abruptly below about 150 K (near T_C), and then levels off to a constant value with lowering temperature. The overall temperature-dependent behavior of FWHM is similar to that of the bulk $\chi(T)$ data. The FWHM is plotted against χ with temperature as an implicit parameter in the inset of the upper panel of Fig. 10. It indeed gives a straight-line behavior over the whole measured temperature range implying that the linewidth traces the bulk $\chi(T)$.

The ^{7}Li NMR shift (K) was extracted from the central peak positions of the spectra in Fig. 9 by using the relation $K(T) = [H_{ref} - H(T)]/H(T)$, where $H(T)$ and H_{ref} are the resonance field of the sample and the nonmagnetic reference sample, respectively. The temperature-dependent NMR shift
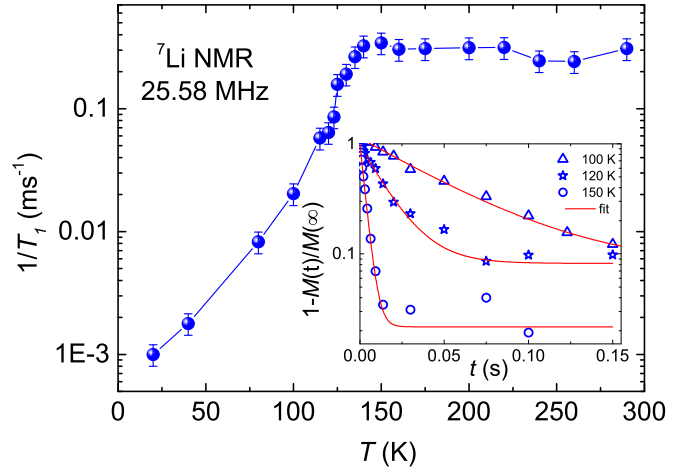

FIG. 11. Spin-lattice relaxation rate $1/T_1$ vs temperature measured at 25.58 MHz. Inset: the longitudinal magnetization recovery curves at various temperatures. The solid lines are the fits, as described in the text.

$[K(T)]$ is presented in the lower panel of Fig. 10. It shows a constant behavior at high temperatures and then increases abruptly below 150 K, suggesting the occurrence of a ferrimagnetic ordering. The overall behavior of $K(T)$ is again similar to that observed for $\chi(T)$ and FWHM(T). Since $K(T)$ measures the intrinsic spin susceptibility $\chi_{spin}(T)$, one can write the relation

$$K(T) = K_{chem} + \frac{A_{hf}}{N_A \mu_B} \chi_{spin}(T), \tag{7}$$

where K_{chem} is the temperature independent chemical shift and A_{hf} is the hyperfine coupling constant between the Li nuclei and electronic (Ni^{2+}, Mn^{4+}) spins. The K vs χ plot with temperature as an implicit parameter is presented in the inset of the lower panel of Fig. 10. It produces a linear behavior in the entire measured temperature range. From the slope of a straight line fit, the transfer hyperfine coupling is evaluated to be $A_{hf} \simeq 672.4$ Oe/μ_B.

2. Spin-lattice relaxation rate $1/T_1$

In order to probe the low energy spin dynamics, ^{7}Li NMR spin-lattice relaxation rate ($1/T_1$) is measured at the field corresponding to the central peak position at different temperatures. The measurements are carried out in the temperature range 4 to 290 K. Recovery of the longitudinal magnetization is monitored after a saturation pulse sequence. Some of the representative recovery curves in the low-temperature regime are shown in the inset of Fig. 11. These recovery curves are fitted by single exponential function [39]

$$1 - \frac{M(t)}{M_0} = A e^{-t/T_1}, \tag{8}$$

where $M(t)$ is the nuclear magnetization at a time t after the saturation pulse and M_0 is the equilibrium magnetization. The $1/T_1$ extracted from the fit is plotted with respect to the temperature in Fig. 11.

At high temperatures ($T \geqslant 160$ K), $1/T_1$ is almost temperature independent. In the paramagnetic regime, where the

temperature is higher than the exchange energy between the spins, the temperature-independent behavior of $1/T_1$ is obvious due to uncorrelated moments [40]. Typically, when one approaches the magnetic transition from high temperatures, $1/T_1$ is anticipated to show a sharp peak or divergence with temperature due to the critical slowing down of the fluctuating moments. Our $1/T_1$ does show a weak anomaly at T_C and then decreases rapidly below T_C. The decrease below T_C indicates the relaxation due to scattering of magnons by the nuclear spins [39].

G. Critical scaling of magnetization

For a better understanding of the magnetic properties, we have performed the critical behavior study of magnetization in the vicinity of critical temperature T_C. Scaling hypothesis suggests that the second-order phase transition near T_C can be characterized by a set of critical exponents (β, γ, and δ) and magnetic equations of state [41]. Spontaneous magnetization $M_S(T)$ at $T < T_C$, zero-field inverse susceptibility $\chi_0^{-1}(T)$ at $T > T_C$, and isothermal magnetization (M vs H) at $T = T_C$ are related to the critical exponents by the following equations:

$$M_S(T) = M_0(-\varepsilon)^{\beta}, \ \varepsilon < 0 \tag{9}$$

$$\chi_0^{-1}(T) = \Gamma(\varepsilon)^{\gamma}, \ \varepsilon > 0 \tag{10}$$

$$M = XH^{1/\delta}, \ \varepsilon = 0 \tag{11}$$

where $\varepsilon = (T - T_C)/T_C$ is the reduced temperature and M_0, Γ, and X are the critical amplitudes.

Usually, the Arrott-Noakes equation of state [42] is employed for a reliable estimation of critical exponents and T_C using magnetic isotherms, which can be written as

$$(H/M)^{1/\gamma} = A\varepsilon + BM^{1/\beta}. \tag{12}$$

According to this equation, for a particular set of β and γ values, $M^{1/\beta}$ vs $(H/M)^{1/\gamma}$ plots should produce a set of parallel straight lines in the high-field region for different temperatures around T_C and the isotherm at $T = T_C$ should pass through origin. The plot of $M^{1/\beta}$ vs $(H/M)^{1/\gamma}$ is often called the modified Arrott plot (MAP) and the exponents reflect the universality class of the spin system. The mean field exponents ($\beta = 0.5$ and $\gamma = 1$) lead to conventional Arrott plot (H/M vs M^2), which is traditionally used for critical behavior analysis [43]. We have measured several magnetic isotherms around the T_C in close temperature steps. To avoid residual magnetization, at each temperature the measurements are done after cooling the sample in zero field from high temperatures (above T_C). Figure 12(a) presents the standard Arrott plots for LNMO. All the curves show a nonlinear behavior and a downward curvature in the high-field region. This indicates that the transition is non-mean-field type and standard Arrott plot (associated with mean field theory) may not be an appropriate way to analyze the critical behavior of this system. Further, the order of phase transition can be determined from the slope of Arrott plots. According to the Banerjee criterion, the positive slope corresponds to a second-order phase transition whereas the negative slope indicates a first-order phase transition [44].

Thus, the positive slope found in Fig. 12(a) confirms second-order nature of the transition.

On the other hand, the MAPs constructed using the critical exponents of 3D Heisenberg model resulted more linear behavior in the high-field region compared the mean field one. Therefore, we took the theoretical values of β and γ for 3D Heisenberg model as the starting trial values to construct MAPs. The linear fits to the MAPs in the high-field regime were extrapolated down to zero field and the values of $M_S(T)$ and $\chi_0^{-1}(T)$ were obtained from the intercepts on the $M^{1/\beta}$ and $(H/M)^{1/\gamma}$ axes, respectively. The temperature-dependent M_S and χ_0^{-1} were fitted by Eqs. (9) and (10), respectively, and the values of β and γ were estimated. These sets of β and γ values were again used to construct a new set of MAPs. This whole process was repeated several times, until we got a set of parallel straight lines in the high-field region with a set of stable β, γ, and T_C values. The final MAPs are shown in Fig. 12(b). The obtained M_S and χ_0^{-1} values are plotted as a function of temperature in Fig. 12(c). The solid lines are the fits using Eqs. (9) and (10), respectively. The fit using Eq. (9) yields $\beta = 0.350(2)$ with $T_C = 125.87(3)$ K and the fit using Eq. (10) yields $\gamma = 1.320(2)$ with $T_C = 125.83(3)$ K. These values are almost equal to the values obtained from the final MAPs ($\beta = 0.350$ and $\gamma = 1.332$). As seen from Fig. 12(b), though straight lines are obtained in the high-field region but significant deviation from linearity was found in the low-field region. This is likely due to the averaging over magnetic domains which are mutually misaligned.

In the next step, Kouvel-Fisher (KF) method is used to determine β, γ, and T_C more accurately [45]. The equations involved in the KF method are

$$M_S(T)\left[\frac{dM_S(T)}{dT}\right]^{-1} = (1/\beta)(T - T_C) \tag{13}$$

and

$$\chi_0^{-1}(T)\left[\frac{d\chi_0^{-1}(T)}{dT}\right]^{-1} = (1/\gamma)(T - T_C). \tag{14}$$

From these two equations, it is apparent that $M_S(T)[dM_S(T)/dT]^{-1}$ vs T and $\chi_0^{-1}(T)[d\chi_0^{-1}(T)/dT]^{-1}$ vs T plots should yield straight lines with slopes $1/\beta$ and $1/\gamma$, respectively. The beauty of this method is that, without any previous knowledge about T_C, one can estimate it from the intercept of the straight-line fits on the temperature axis. The KF plots for LNMO are presented in Fig. 12(d). The critical exponent values evaluated from the KF plots are $\beta = 0.352(3)$ with $T_C = 125.83(6)$ K and $\gamma = 1.314(2)$ with $T_C = 125.84(8)$ K. These values of critical exponents match nicely with the ones obtained from the MAPs, indicating the reliability of the values of critical exponents.

Figure 13 presents the critical isotherm at $T \simeq T_C = 125.6$ K. According to Eq. (11), log$M$ vs log$H$ plot at the critical temperature should produce a straight line with slope $1/\delta$. We have plotted log$M$ vs log$H$ in the inset of Fig. 13 and a straight-line fit results $\delta = 4.77(3)$. One can also estimate δ by using the Widom relation [47]

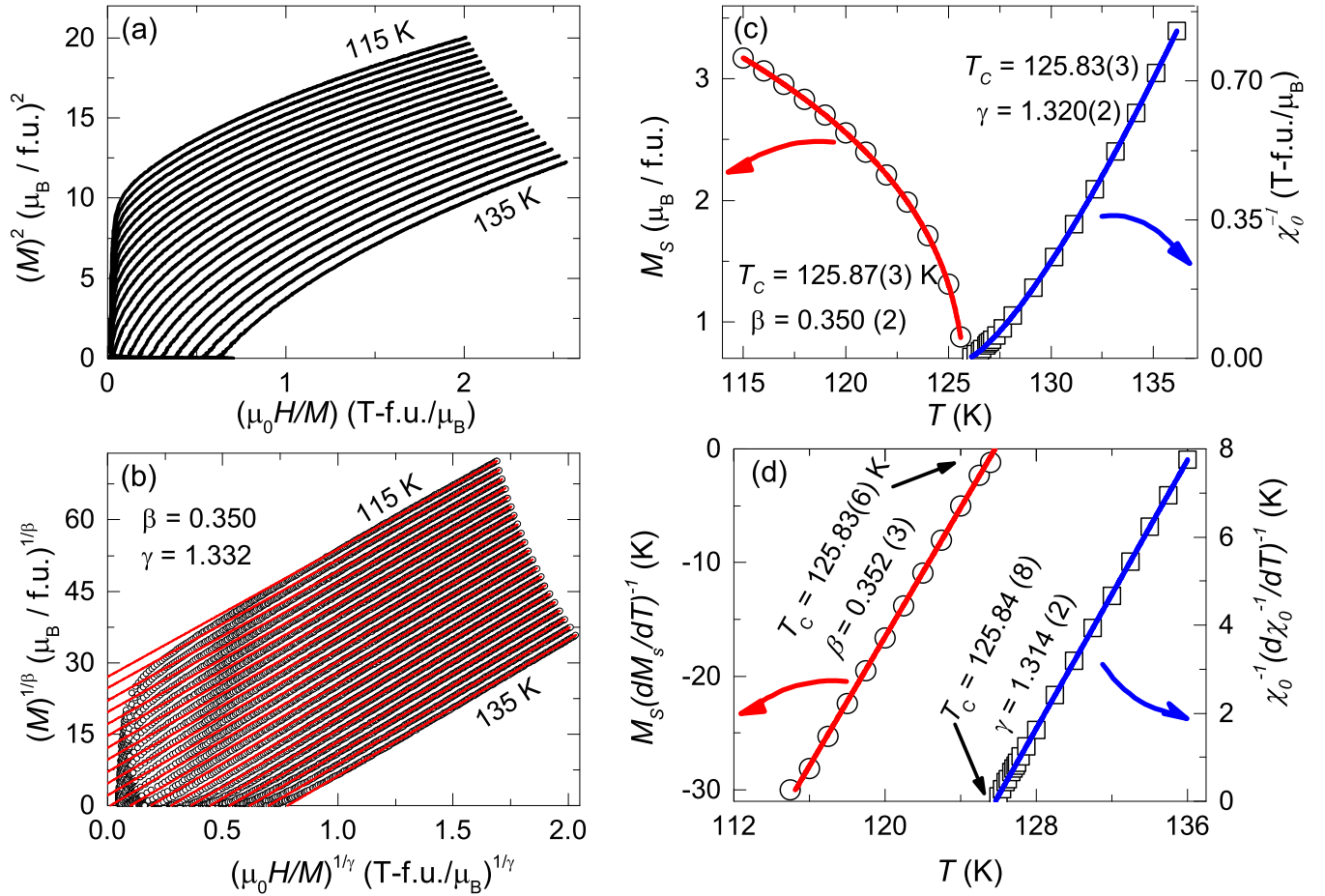$$\delta = 1 + \frac{\gamma}{\beta}. \tag{15}$$

FIG. 12. (a) The Arrott plots (M^2 vs H/M) for LNMO at different temperatures, above and below T_C. (b) The modified Arrott plots [$M^{1/\beta}$ vs $(H/M)^{1/\gamma}$] for LNMO at different temperatures. The solid lines are the linear fits to the data in the high-field regime ($H \geqslant 2.5$ T) and are extrapolated to $H/M = 0$. (c) Spontaneous magnetization M_S and zero-field inverse susceptibility χ_0^{-1} as a function of temperature in the left and right y-axes, respectively, obtained from the intercepts of the modified Arrott plots in the vicinity of T_C. The solid lines are the fits, as described in the text. (d) The Kouvel-Fisher plots for M_S and χ_0^{-1}. The solid lines are the linear fits.

By using the β and γ values from the KF method and MAPs, the corresponding δ value is estimated to be $\delta = 4.733(4)$
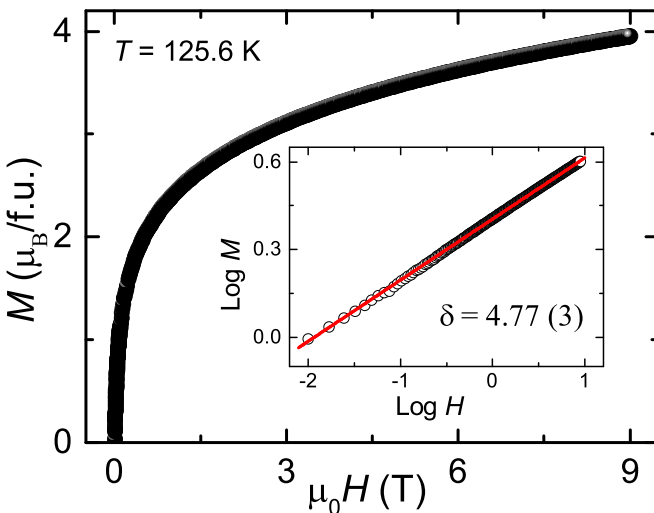

FIG. 13. Magnetization isotherm (M vs H) at $T \simeq T_C$. Inset: log$M$ vs log$H$ plot at $T \simeq T_C$.

and $\delta = 4.771(2)$, respectively. It is found that the δ value obtained from the Widom relation and the critical isotherm analysis are very close to each other, reflecting the self-consistency of our β and γ estimations.

According to scaling hypothesis [46], the obtained critical exponents should follow the universal scaling function

$$M(H, \varepsilon) = \varepsilon^\beta f_\pm \left(\frac{H}{|\varepsilon|^{\beta + \gamma}} \right), \quad (16)$$

where f_+ and f_- are the regular functions for $T < T_C$ and $T > T_C$, respectively. Equation (16) can further be simplified in terms of reduced magnetization (m) and reduced field (h) as

$$m = f_\pm(h), \quad (17)$$

where $m = |\varepsilon|^{-\beta} M(H, \varepsilon)$ and $h = H|\varepsilon|^{-(\beta + \gamma)}$. Equations (16) and (17) suggest that for appropriate choice of critical exponents, all the curves in the m vs h and m^2 vs h/m plots should fall into two separate branches: f_+ for $T > T_C$ and f_- for $T < T_C$. This behavior can be clearly visualized in Fig. 14. In the inset of the upper panel of Fig. 14 we have plotted m vs h in log-log scale which magnify the data in the low-field regime and confirms no dispersion among the curves
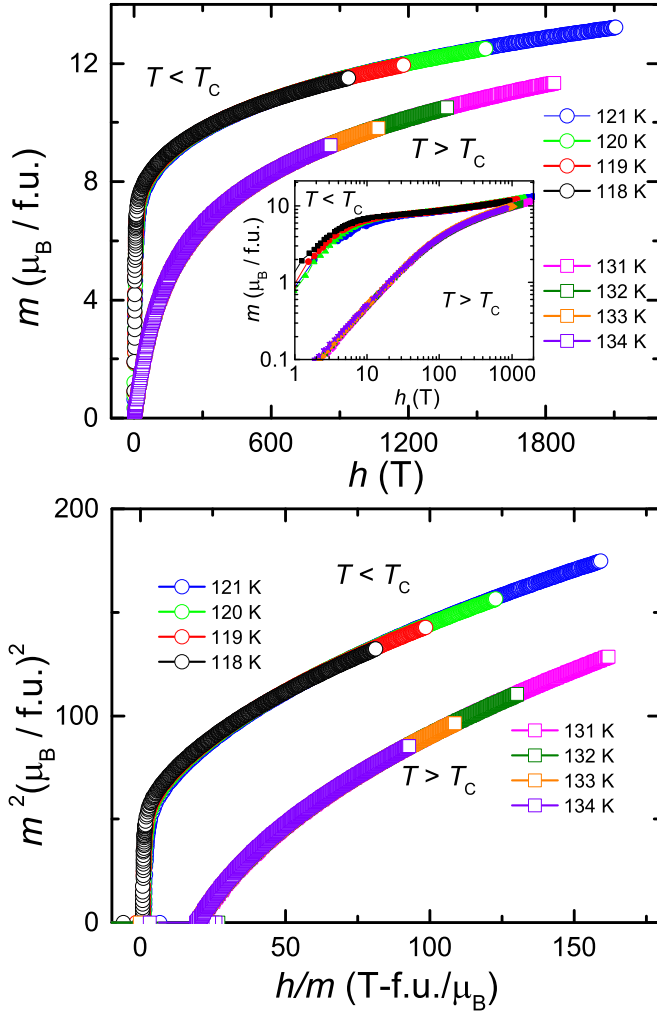
FIG. 14. Upper panel: the reduced magnetization $m = |\varepsilon|^{-\beta}M(H, \varepsilon)$ vs reduced magnetic field $h = H|\varepsilon|^{-(\beta+\gamma)}$. The renormalized curves in different temperatures, just above and below T_C, are collapsing into two separate branches. Inset: the log-log plot of m vs h to magnify the data in the low-field region. Lower panel: m^2 vs h/m plots where the curves just above and below T_C are collapsing into two separate branches.

in two branches. This further confirms the reliability of the estimated critical exponent values.

For a comparison, all the values of critical exponents evaluated by the above methods along with the theoretical values

corresponding to various universality classes (mean field, 3D Heisenberg, 3D Ising, and 3D XY) are listed in Table III. One can see that our estimated critical exponents ($\beta \sim 0.35$, $\gamma \sim 1.32$, and $\delta \sim 4.772$) are very close to the 3D XY model. This implies that LNMO belongs to the 3D XY universality class. This is quite consistent with the magnetic structure deduced from the NPD data where the spin alignments are restricted only to the *ab*-plane. There are certain compounds known to show the evidence of magnetic LRO belonging to the 3D XY universality class, e.g., $CuGeO_3$ [48], Gd_2IFe_2, Gd_2ICo_2, and Gd_2BrFe_2 [49].

H. Magnetocaloric effect

The MCE is defined as the reversible change in temperature of a magnetic material while magnetic field is applied or removed in an adiabatic condition. Generally, isothermal entropy change (ΔS_m) and adiabatic temperature change (ΔT_{ad}) with respect to the change in magnetic field quantify the MCE of a system. From the Maxwell's thermodynamic relation, $(\partial S/\partial H)_T = (\partial M/\partial T)_H$, ΔS_m can be estimated using the magnetization isotherm (M vs H) data as

$$\Delta S_m(H, T) = \int_{H_i}^{H_f} \frac{dM}{dT}dH. \tag{18}$$

Figure 15(a) presents the 3D plot of ΔS_m with the change in field (H) and temperature (T). ΔS_m changes gradually with H and shows a maximum entropy change across the T_C, with a highest value of $\Delta S_m \simeq 11.2$ J/kg K for 9-T field change. Furthermore, ΔT_{ad} is calculated from the zero-field heat capacity and magnetization isotherms using the relation

$$\Delta T_{ad} = -\int_{H_i}^{H_f} \frac{T}{C_p}\frac{dM}{dT}dH. \tag{19}$$

The 3D plot of ΔT_{ad} as a function of H and T is shown in Fig. 15(b). ΔT_{ad} shows a gradual temperature evolution with respect to H showing a maximum value ~4 K for 9 T field change near T_C. The shape of both $\Delta S_m(T)$ and $\Delta T_{ad}(T)$ peaks appear to be asymmetric and expanded over a wide temperature range around T_C.

Another important parameter which is very useful to evaluate the performance of a magnetocaloric material is relative cooling power (RCP). It defines the amount of heat transfer between its hot and cold reservoirs which can be written

TABLE III. Experimentally evaluated critical exponents (β, γ, and δ) and T_C for LNMO obtained from MAP, KF plot, critical isotherm analysis, and MCE. For a comparison, the theoretically predicted values for different universality classes (mean field, 3D Heisenberg, 3D Ising, and 3D XY) are also listed (taken from Ref. [46]).

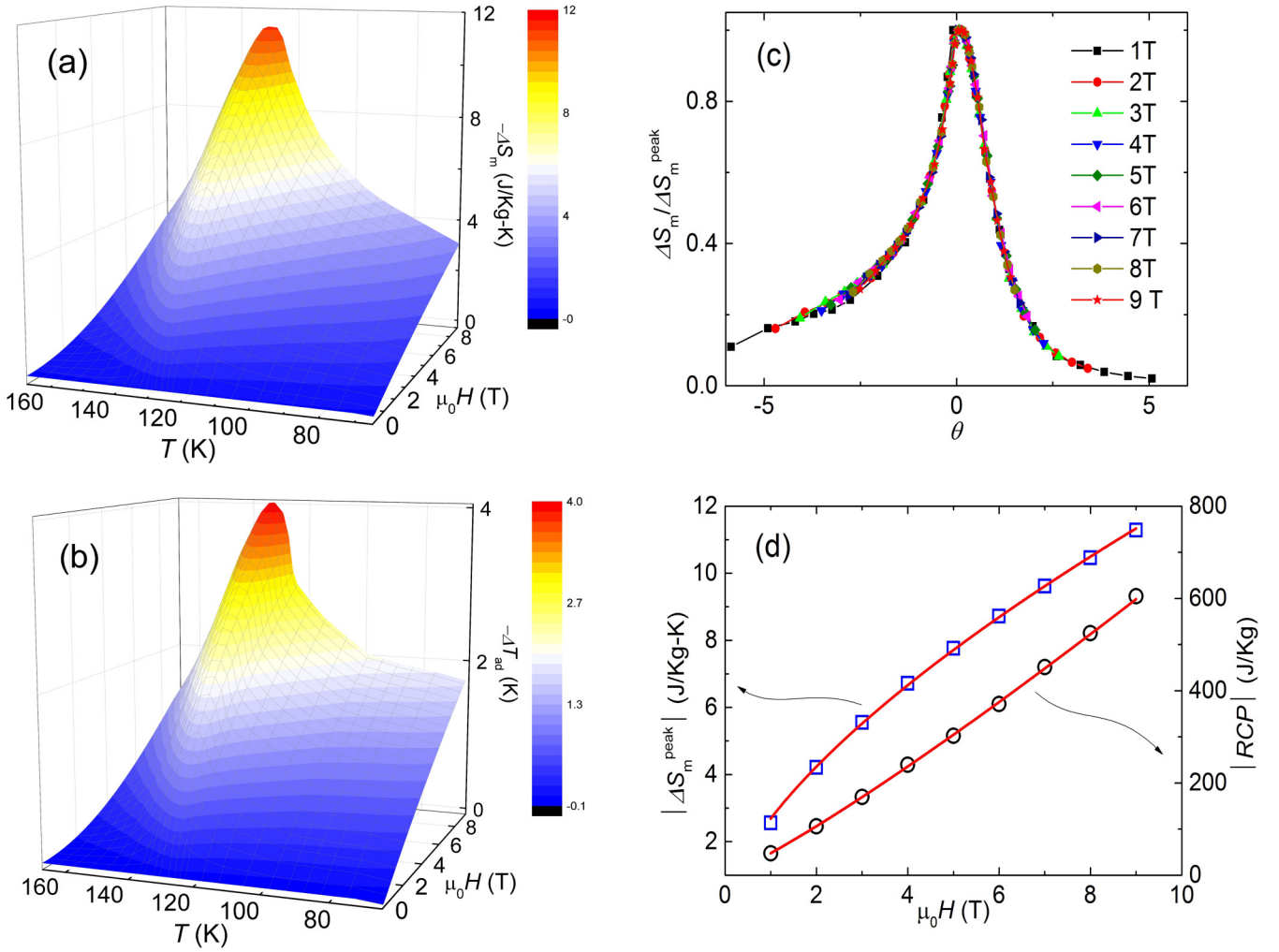| Parameters	MAP	KV plot	Critical isotherm analysis	MCE	Mean field model	3D Heisenberg model	3D XY model	3D Ising model
β	0.350(2)	0.352(3)			0.5	0.365	0.345	0.325
γ	1.320(2)	1.314(2)			1	1.386	1.316	1.241
δ	4.771(2)	4.733(4)	4.77(3)	4.72(9)	3	4.80	4.80	4.82
n	0.61(2)	0.61(3)		0.61(2)				
T_C (K)	125.83(3)	125.84(8)	125.6					

FIG. 15. (a) The isothermal change in magnetic entropy (ΔS_m) as function of temperature (T) and field (H). (b) The adiabatic change in temperature (ΔT_{ad}) as a function of temperature (T) and field (H). (c) Universal curve plot of normalized entropy change as a function of θ with the application of 1 to 9 T magnetic field change. (d) Absolute value of entropy change at the peak position ΔS_m^{peak} and relative cooling power (RCP = $\Delta S_m^{peak} \times \delta T_{FWHM}$) as a function of magnetic field in the left and right y-axes, respectively. Solid lines are the fits as described in the text.

mathematically as

$$\text{RCP} = \int_{T_{cold}}^{T_{hot}} \Delta S_m(T, H) dT. \qquad (20)$$

Here, T_{cold} and T_{hot} are the temperatures corresponding to the cold and hot reservoirs, respectively. Thus, RCP can be evaluated approximately as

$$|\text{RCP}|_{approx} = \Delta S_m^{peak} \times \delta T_{FWHM}, \qquad (21)$$

where ΔS_m^{peak} is the peak value and δT_{FWHM} is the full width at half-maximum (FWHM) of the $\Delta S_m(T)$ curves in Fig. 15(a). The highest value RCP is found to be ∼604 J/Kg for 9 T field change. This value of RCP is quite high and comparable to other well-known magnetocaloric materials, having T_C around this temperature.

In Table IV, we have made a comparison of the RCP and ΔS_m^{peak} values of LNMO with some other magnetocaloric materials with T_C = 110–140 K. In most of the materials with

second-order phase transition, the shape of the ΔS_m curves is broad and asymmetric which is one of the main reasons for the large value of RCP. Although, materials with first-order phase transition show giant MCE and large ΔS_m and ΔT_{ad} values but the width of these peaks are narrow, which restricts the usability of these materials for a cyclic operation. Another drawback is that the materials with first-order phase transition show hysteretic behavior which leads to energy loss [50]. Therefore, materials with second-order phase transition are more preferred for the magnetic refrigeration purpose than the ones with first-order phase transition. It has been theoretically predicted that geometrically frustrated magnets could show enhanced MCE compared to the ordinary nonfrustrated magnets [51]. In particular, pyrochlore lattices are predicted to show highest MCE among the geometrically frustrated lattices. Subsequently, this idea has been utilized to design several new magnetocaloric materials with strong spin fluctuations and/or frustration [52,53]. Indeed, LNMO is a frustrated pyrochlore magnet and hence the asymmetric behavior can

TABLE IV. Comparison of experimental ΔS_m^{peak} and RCP values for LNMO with some reported magnetocaloric materials having $T_C = 110$–140 K for a field change of 5 T.

System	T_C (K)	Nature of transition	ΔS_m^{peak} (J/Kg K)	RCP (J/Kg)	Ref.
Tb_2NiMnO_6	110	Second order	5.2		[54]
DyGa	113	Second order	5.8	381.9	[55]
$LiNi_{0.5}Mn_{1.5}O_4$	125.8	Second order	7.76	302	This work
$GdCo_{0.2}Mn_{1.8}$	140	Second order	4.11	320	[56]
$Tb_5Ge_{2-x}Si_{2-x}Mn_{2x}, 2x = 0.1$	123	First order	20.84	330.43	[57]
$Dy(Co_{0.98} Ni_{0.02})_2$	126	First order	11	304	[58]
$YFe_2H_{4.2}$	132	First order	7.11	263	[59]

be attributed to the effect of magnetic frustration. Thus, the obtained large ΔS_m and RCP values make LNMO a promising compound for magnetic refrigeration purpose.

Further, MCE can also be utilized to gain more insight about the nature of the magnetic phase transition and the critical exponents. The universal scaling curve construction of ΔS_m proposed by Franco *et al.* [60] is generally used for this purpose. This method is tested on a variety of materials and found to be a very efficient way of investigating the nature of the phase transition [61]. To construct the universal scaling curves, first we normalized all the $\Delta S_m(T)$ curves with their respective peak values (i.e., $\Delta S_m/\Delta S_m^{peak}$) for each field change and then plotted as a function of θ in Fig. 15(c). Here, θ is the rescaled temperature which is given by

$$\theta = -(T - T_C)/(T_{r1} - T_C) \text{ for } T \leqslant T_C \quad (22)$$

and

$$\theta = (T - T_C)/(T_{r2} - T_C) \text{ for } T > T_C. \quad (23)$$

In the above, T_{r1} and T_{r2} are the two reference temperatures corresponding to $0.5 \times \Delta S_m^{peak}$ values and $T_C \simeq 125.8$ K (obtained from the Kouvel-Fisher plot). As it is seen from Fig. 15(c), all the normalized curves for different field changes collapse into a single curve similar to the other reported compounds showing second-order phase transition [61,62].

The ΔS_m^{peak} and RCP values are plotted in Fig. 15(d), as a function of field in the left and right *y*-axes, respectively. For the purpose of critical analysis, we have fitted the field-dependent ΔS_m^{peak} and RCP curves by the following power laws [60]:

$$\left| \Delta S_m^{peak} \right| \propto H^n \quad (24)$$

and

$$|RCP| \propto H^{(1+1/\delta)}. \quad (25)$$

The fit of Eq. (24) to the ΔS_m^{peak} vs T data yields $n = 0.61(2)$. The exponent n is related to the critical exponents β and γ by the relation

$$n = 1 + \left(\frac{\beta - 1}{\beta + \gamma} \right). \quad (26)$$

Using β and γ values obtained from the modified Arrot plot and Kouvel-Fisher plots, the value of n is estimated to be 0.61(2) and 0.61(3), respectively. These values of n obtained from various analysis methods are consistent with each other

and confirm the reliability of our critical analysis technique. Similarly, the fit of RCP vs H data using Eq. (25) yields $\delta = 4.72(9)$, which is consistent with the values obtained from modified Arrott plot, Kovel-Fisher plot, and critical isotherm analysis techniques. A more quantitative analysis of the phase transition can be done by using the method proposed recently by Law *et al.* [63]. The exponent n in Eq. (24) is normally field and temperature dependent and can also be calculated locally as

$$n(T, H) = \frac{d \ln|\Delta S_m|}{d \ln H}. \quad (27)$$

We used Eq. (27) to quantify the local H and T variation of exponent n and plotted as a 3D plot in Fig. 16. Since in the low-field range, the system has multidomain states, we have shown only the values corresponding to high fields ($\mu_0 H > 2$ T) in Fig. 16. At low temperatures ($T < T_C$), the n vs T curve is found to be almost constant and n approaches a value ~ 0.94 which is close to 1. As the temperature is increased, n decreases smoothly and passes through a minima at $T \simeq T_C$ with $n = 0.61(1)$. At high temperatures, it increases almost linearly and reaches up to a value $n = 1.98$ which is close to 2. At $T = T_C$, the value of n depends on the value of other critical exponents of the material, as they are connected by Eq. (26).
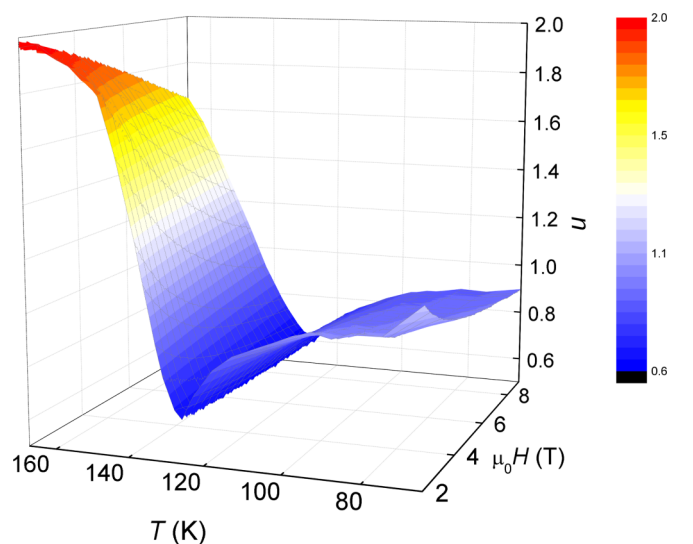

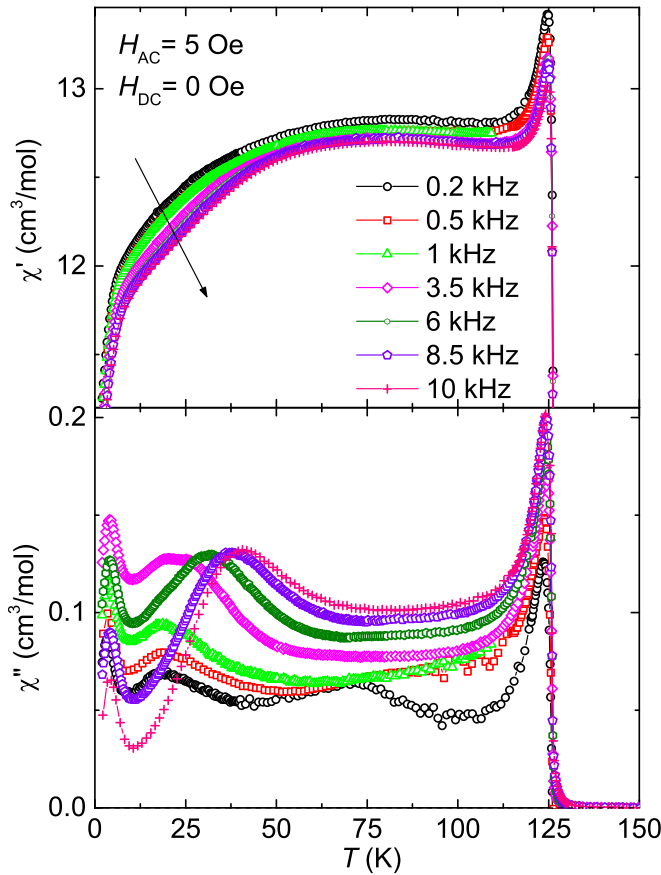FIG. 16. Field and temperature dependence of the exponent n using Eq. (27).

FIG. 17. Upper panel: real part of the ac susceptibility χ' vs temperature at different frequencies. The arrow points to the change in χ' with frequency. Lower panel: imaginary part of the ac susceptibility χ'' vs temperature at different frequencies.
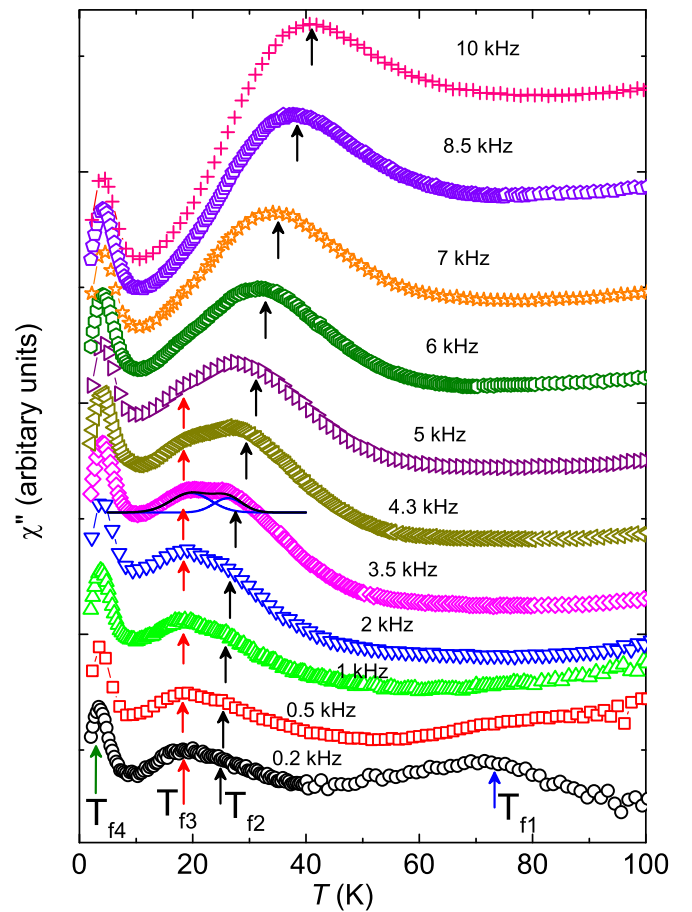

FIG. 18. Enlarged view of $\chi''(T)$ at low temperatures and at different frequencies. The curves are vertically translated to get a clear view of the peak positions. The vertical arrows guide the peak positions with frequency.

The overall behavior of n vs T curve (with exponent value, $n < 2$) is found to be similar to other compounds showing second-order phase transition [63].

I. ac susceptibility

Figure 17 presents the temperature-dependent ac susceptibility measured in different frequencies and at a fixed ac field of $H_{ac} \simeq 5$ Oe. As shown in the upper panel of Fig. 17, the real part of the ac susceptibility (χ') shows a sharp peak at $T_C \simeq 125$ K and below 50 K it decreases with temperature, akin to the behavior observed in the ZFC dc $\chi(T)$ (inset of Fig. 5). The peak at 125 K is almost frequency independent indicating the onset of long-range ferrimagnetic order. Another broad feature appears at around 25 K in low frequencies and the absolute value of χ' at this temperature is found to be reduced with increasing frequency (indicated by a downward arrow). The imaginary part of the ac susceptibility (χ'') is shown in the lower panel of Fig. 17 as a function of temperature. Similar to the $\chi'(T)$ data, $\chi''(T)$ also shows a sharp peak at T_C which is frequency independent. At low temperatures, $\chi''(T)$ shows various anomalies and some of them are frequency dependent. To clearly visualize those low-temperature features, $\chi''(T)$ data at different frequencies are vertically translated and magnified in Fig. 18. At the lowest measured frequency of

0.2 kHz, $\chi''(T)$ below T_C exhibits two broad humps at ~ 72 K and ~ 20 K and a narrow peak at ~ 3.5 K, as indicated by the upward arrows. The broad hump at $T_{f1} \sim 72$ K disappears as the frequency is increased beyond 0.5 kHz. With a very careful observation, we found that the broad hump near 20 K consists of two shoulderlike features, one at $T_{f2} \simeq 18$ K and another at $T_{f3} \simeq 20$ K. As the frequency is increased, the shoulder at T_{f2} becomes more pronounced and shifts toward high temperatures, reflecting a glassy behavior. On the other hand, the shoulder at T_{f3} remains frequency independent and gets diminished at high frequencies. Similarly, the peak at $T_{f4} \sim 3.5$ K also remains unaltered with frequency indicating that it could be an AFM transition. The multiple magnetic transitions in the ordered state can be attributed to the effect of magnetic frustratio [64]. The absence of these features in χ' can be believed as a consequence of large value of χ' associated with ferrimagnetism [65].

Since all the peaks are frequency independent except one, we focused our analysis only on the frequency-dependent peak at T_{f2}. The peak positions of T_{f2} and T_{f3} are extracted by a double Gaussian fit (shown in Fig. 18 for 3.5 kHz). The relative shift of freezing temperature (T_{f2}) with frequency (ν) can be quantified by calculating the Mydosh parameter δT_f,

given by [66]

$$\delta T_f = \left(\frac{\Delta T_{\mathrm{f}}}{T_{\mathrm{f}} \Delta (\log_{10} \nu)} \right), \tag{28}$$

where $\Delta T_{\mathrm{f}} = (T_{\mathrm{f}})_{\nu_1} - (T_{\mathrm{f}})_{\nu_2} \simeq 16.65$ K and $\Delta \log_{10}(\nu) = \log_{10}(\nu_1) - \log_{10}(\nu_2)$. Here, ν_1 and ν_2 are taken as the lowest (200 Hz) and highest (10 kHz) measured frequencies, respectively. For LNMO, the Mydosh parameter is estimated to be $\delta T_f \simeq 0.4$, which is found to be two orders of magnitude higher than the value for canonical SG systems [e.g., AuMn, $(\delta T_f \simeq 0.0045)$] [67] and one order magnitude higher than the cluster SG systems [e.g., $Cr_{0.5}Fe_{0.5}Ga$, $(\delta T_f \simeq 0.017)$] [22]. However, it lies in the range of a superparamagnet [e.g., $\alpha - (Ho_2O_3B_2O_3)$, $(\delta T_f \simeq 0.28)$] [66].

To understand the frequency dependence of T_{f2} and the correlation among the magnetic entities we analyzed the data using various theoretical models. At first, we tried to fit the data using Arrhenius law [68]

$$\tau = \tau_0 \exp\left(\frac{E_{\mathrm{a}}}{k_{\mathrm{B}} T_{\mathrm{f}}} \right), \tag{29}$$

where τ is the timescale of dynamical fluctuation, τ_0 is the relaxation time for the single spin flip, $E_{\mathrm{a}}/k_{\mathrm{B}}$ is the activation energy required to overcome the energy barrier by which the metastable states are separated, and τ_0 is the time taken to overcome the energy barrier. In the upper panel of Fig. 19, we have plotted $\ln \tau$ vs $1/T_{f2}$. Clearly, it shows a change in slope at around 27 K. In the high-temperature ($T > 27$ K) region, the data could be fitted well by Eq. (29) resulting $E_{\mathrm{a}}/k_{\mathrm{B}} \simeq 61.7$ K and $\tau_0 \simeq 3.7 \times 10^{-6}$ s. Such an Arrhenius behavior is often considered to be the characteristic feature of superparamagnetism [69]. The value of τ_0 also seems to be within the range expected for superparamagnets (10^{-6} to 10^{-9} s) [70].

In the low-temperature ($T < 27$ K) region, the data show a significant deviation from the Arrhenius law as evident in the upper panel of Fig. 19. This indicates that there are two different relaxation mechanisms involved. We fitted the low-T data by the dynamical scaling law or power law, predicted for SG systems [71]

$$\tau = \tau' \exp\left(\frac{T_{f2}}{T_{\mathrm{g}}} - 1 \right)^{-z\nu'}. \tag{30}$$

Here, τ' has the same physical meaning as τ_0, T_{g} is the freezing temperature as ν approaches zero, and $\tau' = \xi^z$ with z being the dynamical critical exponent. The correlation length has the form $\xi = (T_{f2}/T_{\mathrm{g}} - 1)^{-\nu'}$ with critical exponent ν'. Equation (30) can be rewritten in a simplified form as

$$\log_{10} \tau = \log_{10} \tau' - z\nu' \log_{10}\left(\frac{T_{f2}}{T_{\mathrm{g}}} - 1 \right). \tag{31}$$

As shown in the lower panel of Fig. 19, Eq. (31) fits well to the low-T data giving $\tau' \simeq 5.08 \times 10^{-9}$ s and $z\nu' \simeq (6.6 \pm 0.2)$. In the fitting process we have fixed $T_{\mathrm{g}} \simeq (21.03 \pm 0.01)$ K, obtained from the y-intercept of the linear fit of T_{f2} vs $\log_{10} \nu$ plot (see the inset of lower panel of Fig. 19). The larger value of τ' clearly indicates that the spin dynamics is slower than conventional SG systems ($\sim 10^{-13}$ s) [66]. Such a high value of τ' is previously reported for various reentrant-SG
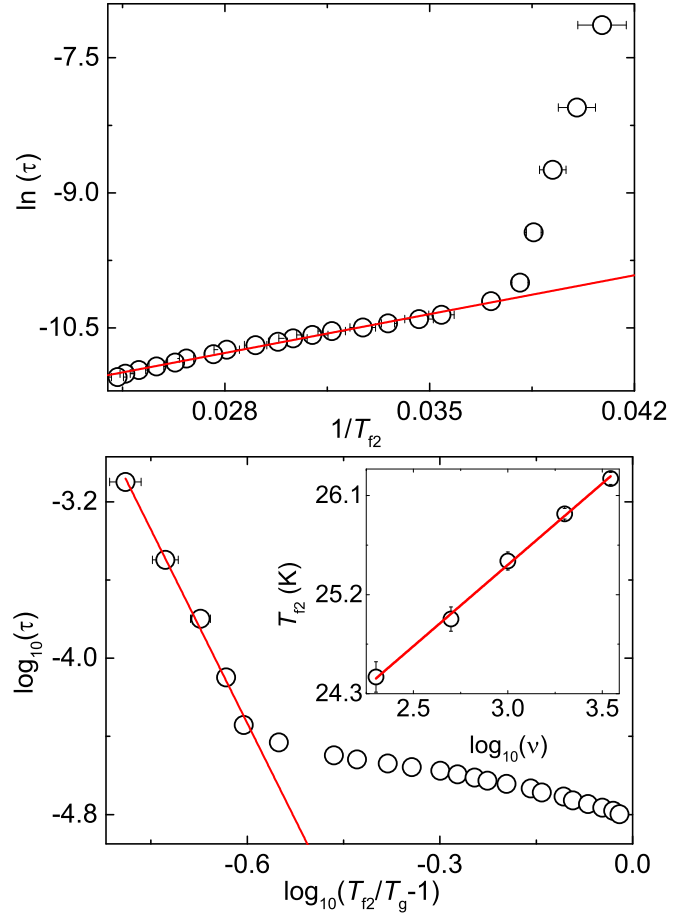

FIG. 19. Upper panel: $\ln(\tau)$ vs $1/T_{f2}$ plot. The solid line is the fit using Eq. (29) in the high-temperature region. Lower panel: $\log_{10}(\tau)$ vs $\log_{10}(T_{f2}/T_{\mathrm{g}} - 1)$ plot. The solid line is the fit using Eq. (31). Lower inset: T_{f2} vs $\log_{10} \nu$ plot in the low-temperature region. The solid line is the fit as described in the text.

systems [70,72]. Further, the value of $z\nu'$ also falls in the range expected for typical SG systems ($z\nu' \simeq 4 - 12$) and comparable to the values reported for various reentrant-SG systems [70,72].

Thus, the frequency dependence of T_{f2} follows an Arrhenius behavior at higher temperatures which could suggest that the system is superparamagnet far above the critical region ($T \gg T_{\mathrm{g}}$). As we move closer to T_{g}, Arrhenius behavior breaks down and power-law behavior takes over which evidences the existence of SG transition at $T_{\mathrm{g}} \simeq 21.03$ K, similar to the dilute magnet $LiHo_xY_{1-x}F_4$ ($x = 0.045$) [73]. In order to resolve this ambiguity, memory effect measurements are discussed later.

J. Nonequilibrium dynamics

1. Magnetic relaxation

To explore the low-temperature spin dynamics in LNMO, we have performed the magnetic relaxation time measurement at different temperatures (2, 10, and 70 K), below T_{b}. The sample was cooled in ZFC condition from high-temperature paramagnetic state ($T \geqslant 200$ K) to the desired temperature. After waiting for $t_{\mathrm{w}} = 60$ s at the desired temperature, a
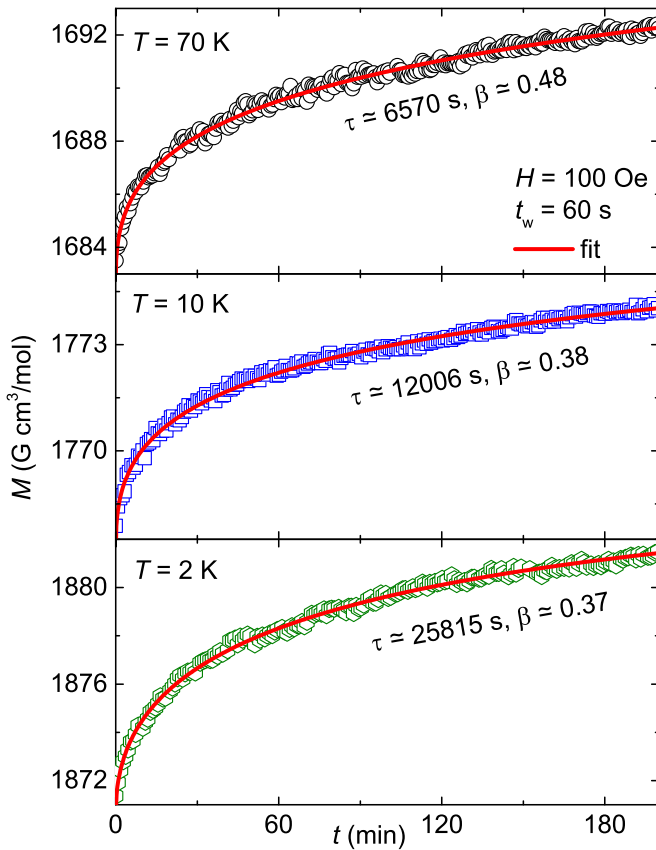
FIG. 20. Time dependence of ZFC magnetization at different temperatures ($T = 2$, 10, and 70 K) in $H = 200$ Oe and after a waiting time of 60 s. The solid lines are the fits using Eq. (32).

small magnetic field of $H \simeq 100$ Oe is applied. Thereafter, the growth of the magnetization with time [$M(t)$] was recorded. The resulting $M(t)$ curves are plotted in Fig. 20. The time evolution of magnetization curves is found to follow a stretched exponential behavior specified by the Kohlrausch-Williams-Watts relation [74,75]

$$M(t) = M_0 - M_g \exp[-(t/\tau)^\beta]. \quad (32)$$

Here, M_0 is the intrinsic magnetization at $t = 0$, M_g is associated with the glassy component of the magnetization, τ is the characteristic relaxation time, and β is the stretching exponent. Typically, the value of β varies between 0 and 1 which decides the dynamics of a spin system. β is also a function of temperature and is strongly dependent on the nature of energy barrier involved in the relaxation process. Following Eq. (32), when $\beta = 0$, $M(t) =$ constant: means no relaxation. Similarly, $\beta = 1$ implies relaxation of a spin system with a single time constant due to the presence of uniform energy barrier. On the other hand, $\beta < 1$ implies the presence of the distribution of nonuniform energy barriers, typically observed for SG and superparamagnetic systems [22,24,74,76].

The $M(t)$ curves for $T = 70$, 10, and 2 K are well fitted by Eq. (32), yielding $\beta \simeq 0.48$, 0.38, and 0.37, respectively. These values are less than 1 suggesting the evolution of magnetization through a number of intermediate metastable states. The value of τ increases with decreasing temperature as expected for glassy systems [22,77]. The relaxation

behavior observed at $T = 10$ and 2 K is quite natural because both of these temperatures are well below T_{f2}. However, the slow relaxation behavior observed at high temperatures ($T = 70$ K $> T_{f2}$) is unusual and suggests that the persistence of SG/superparamagnetism beyond T_{f2} in the ferrimagnetically ordered state.

2. Magnetic memory effect

Since the bifurcation of the dc ZFC and FC $\chi(T)$ data occurs for both SG and superparamagnetic systems, the history dependent measurements are required in order to delineate the microscopic character of the spin system. Therefore, in the following, we have described the magnetic memory effect measurements in both FC and ZFC protocols.

In the FC protocol, the sample was cooled in a small magnetic field of $H = 100$ Oe from high-temperature paramagnetic state ($T \geqslant 200$ K) to the lowest measured temperature $T = 2$ K at a constant rate of 0.5 K/min with intermediate stops at three different temperatures ($T_1^w = 70$ K, $T_2^w = 12$ K, and $T_3^w = 5$ K). At each stop, the magnetic field was switched off and a waiting time of $t_w = 3$ h was given for the magnetization to relax. After each t_w, the same magnetic field was applied and field-cooled cooling (FCC) process was resumed. In this way, the recorded magnetization (M_{FCC}^w) is plotted in the upper panel of Fig. 21 which shows steplike features at each stopping temperature. Once it reached 2 K, the magnetization was recorded by heating the sample at the same rate (0.5 K/min) back to 200 K in the same magnetic field without any intermediate stop. The resulting field-cooled warming magnetization data are referred as M_{FCW}^{mem} in the upper panel of Fig. 21. As depicted in the inset of the upper panel of Fig. 21, M_{FCW}^{mem} also exhibits change of slope at each stopping temperature ($T_2^w = 12$ K and $T_3^w = 5$ K) as in M_{FCC}^w. These characteristic features clearly imply that the system tries to remember the thermal history of magnetization during cooling, thus, showing the magnetic memory. A weak change of slope was also seen at the stopping temperature $T_1^w = 70$ K which is well above T_{f2}. Similar behavior is also reported for reentrant SG compound Lu$_2$MnNiO$_6$ and it is mentioned that the unusual behavior where memory exists above T_f and below T_C can be attributed to the effect of magnetic frustration due to competing FM and AFM interactions [38]. A FCC curve M_{FCC}^{ref} in the same field without any interruption is also measured as a reference.

In the ZFC protocol, the sample was cooled in zero magnetic field form $T \geqslant 200$ to 2 K at a constant rate of 0.5 K/min with three intermediate stops at $T_1^w = 70$ K, $T_2^w = 12$ K, and $T_3^w = 5$ K. At each stop, the sample was allowed to relax for a waiting time of 3 h. After reaching 2 K, the magnetization M_{ZFCW}^{mem} was collected by warming the sample up to 200 K, after applying a small magnetic field of 100 Oe. The reference data M_{ZFCW}^{ref} were also taken by measuring the magnetization during warming in the same magnetic field 100 Oe, after the sample was cooled in zero magnetic field without any intermediate stop. From the data presented in the lower panel of Fig. 21, it can be seen that there is neither any clear dip nor any change in slope in the M_{ZFCW}^{mem} data at the stopping temperatures, implying the absence of ZFC memory effect. The difference in magnetization $\Delta M (= M_{ZFCW}^{mem} - M_{ZFCW}^{ref})$ vs
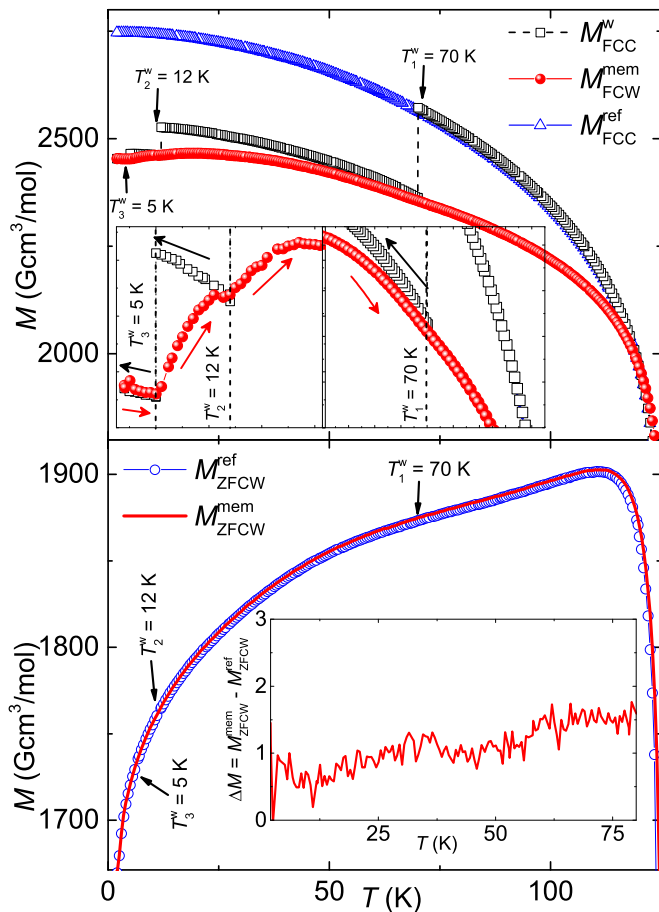
FIG. 21. Memory effect measured as a function of temperature in FC (upper panel) and ZFC (lower panel) protocols in $H = 100$ Oe, as described in the text. Inset of the upper panel magnifies the features at the interruption points: $T = 5$, 12, and 70 K. The difference in magnetization $\Delta M (= M_{ZFCW}^{mem} - M_{ZFCW}^{ref})$ vs T is plotted in the inset of the lower panel.

T is also plotted in the inset of the lower panel of Fig. 21 to highlight no memory effect. In order to make sure that there is no ZFC memory, we have also studied memory effect by measuring ac susceptibility in the ZFC protocol, following the same procedure as discussed above. Similar to the dc $\chi(T)$, the real (χ') and imaginary (χ'') parts of the ac susceptibility data (not shown) do nt show any change of slope at the stopping temperatures. This further proves that no memory is imprinted by aging under zero field.

The above memory effect can be understood from the simple two-state model proposed by Sasaki *et al.* [25] and Tsoi *et al.* [24] for noninteracting magnetic nanoparticles (superparamagnets). In this model, it is assumed that a superspin associated with the dipole magnetic moment of a nanoparticle can occupy one of the two states with energies $-KV \pm HM_s V$, where K is the bulk anisotropy constant, V is the volume of the nanoparticle, and H is the applied field. Therefore, a broad distribution of particle volumes results in a broad distribution of anisotropic energy barriers. The occupation probability $p_1(t)$ of one of the two states, in which the superspin is antiparallel or parallel to the applied field, is $p_1(t) = 0.5$ [i.e. $M(t) = 0$] at any time t, if $p_1(t = 0) = 0.5$

and $H = 0$. Thus, in a ZFC process, which starts from a initial demagnetized state [$M(t = 0) = 0$], $p_1(t)$ and hence the total magnetization is independent of the waiting time (t_w), whereas for a FC process which starts from a initial magnetized state, $p_1(t)$ and hence the total magnetization is dependent on t_w. In light of this model, a superparamagnet should not show ZFC memory but it can show FC memory simply because of the blocked (frozen) superspins. On the other hand, a SG system can show both FC and ZFC memories which are well explained by Sasaki *et al.* [25] considering the random energy model [78] as well as the droplet theory [79] proposed for SG systems. The above models have been employed to describe the experimental data of various superparamagnets and SG systems [24–27]. Thus, the absence of ZFC memory discriminates the dynamics of LNMO from the behavior of a SG and establishes the superparamagnetic nature at low temperatures [24,76]. It is quite surprising that despite having large average particle sizes ($\sim$100 nm), the compound still behaves like a superparamagnet. It is to be noted that the unconventional superparamagnetism is also reported in several compounds in polycrystalline form [80].

3. Memory effect using magnetic relaxation

To investigate the memory effect in further detail, we have performed the magnetic relaxation measurements following the protocol reported by Sun *et al.* [81] for both negative and positive T-cycles.

Negative T-cycle. In a negative temperature cycle, we have measured the magnetic relaxation in both ZFC and FC protocols and are plotted in Figs. 22(a) and 22(b), respectively. In the ZFC procedure, the sample was first cooled from 200 K down to 12 K in zero field. At 12 K, a small field of 100 Oe was applied and $M(t)$ was recorded for $t_1 = 2$ h, which is found to grow exponentially with t. The sample was again cooled down to 5 K in the same magnetic field and $M(t)$ was measured for $t_2 = 2$ h. The nature of $M(t)$ curve was found to be almost constant with t. Thereafter, the temperature was restored back to 12 K and $M(t)$ was recorded for $t_3 = 2$ h in the same field. At this temperature, the $M(t)$ curve was again found to grow exponentially with t. As shown in the inset of Fig. 22(a), the $M(T)$ data measured during t_1 and t_3 follow a continuous growth curve. In the FC process, the sample was cooled in a small magnetic field of 100 Oe down to 12 K. Once it reached 12 K, the magnetic field was switched off and the decay of magnetization with t was measured for $t_1 = 2$ h. The sample was further cooled down to 5 K in zero field and $M(t)$ was recorded for $t_2 = 2$ h at 5 K. This $M(t)$ curve was found to be almost constant with t. Subsequently, the sample was heated back to 12 K in zero field and $M(t)$ was recorded for $t_3 = 2$ h at 12 K. The $M(t)$ curve measured during t_3 was found to decay exponentially with t as a continuation of $M(t)$ curve recorded during t_1 [see the inset of Fig. 22(b)].

Thus, the continuous growth and decay of magnetization during t_1 and t_3 obtained for the ZFC and FC processes, respectively, indicate that the state of the system at 12 K is recovered after a temporary cooling. This a clear demonstration of the memory effect where the system tries to remember the initial state even after going through a change
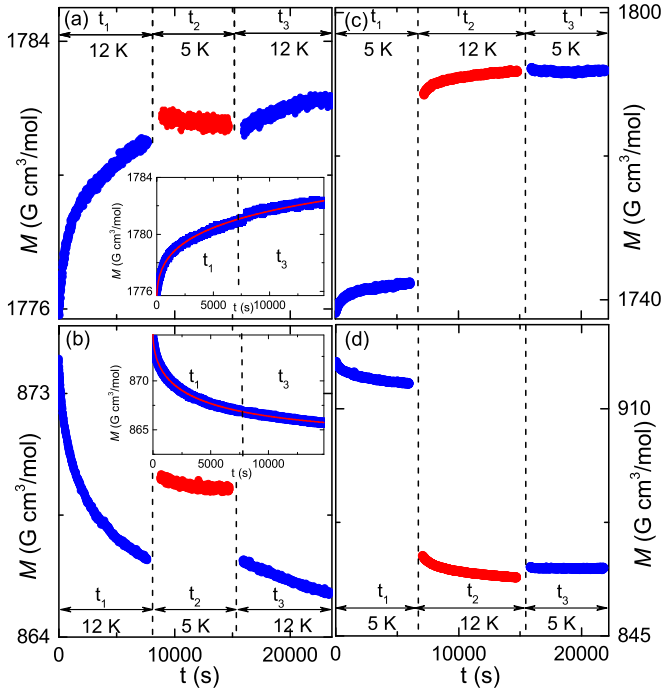
FIG. 22. Magnetic relaxation measured in negative T-cycle for (a) ZFC and (b) FC methods, as described in the text. Insets: magnetic relaxation at 12 K measured during t_1 and t_3 for negative T-cycle and in ZFC and FC methods. The solid lines are the fits using Eq. (32). Magnetic relaxation data measured in positive T-cycle for ZFC and FC methods are shown in (c) and (d), respectively.

of magnetization. These continuous curves could be fitted well by the stretched exponential function [Eq. (32)] with $\beta \simeq 0.37$ and 0.48 for the ZFC and FC processes, respectively, which are consistent with the magnetic relaxation measurements.

Positive T-cycle. Similar to the negative T-cycle, we have also done magnetic relaxation measurements in positive T-cycle in both ZFC and FC protocols. For ZFC procedure, the sample was first cooled from 200 K down to 5 K in zero magnetic field and $M(t)$ was recorded for $t_1 = 2$ h, after applying a small magnetic field of 100 Oe. Then, the sample was heated up to 12 K in the same field and $M(t)$ was measured for $t_2 = 2$ h. Thereafter, the sample was again cooled back to 5 K in the same field and $M(t)$ was recorded for $t_3 = 2$ h. In the FC procedure, the sample was first cooled down to 5 K in a small magnetic field of 100 Oe. Once the temperature reached 5 K, the magnetic field was switched off and $M(t)$ was recorded for $t_1 = 2$ h. By keeping the field zero, the sample was heated to 12 K and $M(t)$ was recorded for $t_2 = 2$ h. In zero field, the sample was further brought back to 5 K and $M(t)$ was measured for $t_3 = 2$ h. The measured ZFC and FC data are presented in Figs. 22(c) and 22(d), respectively. Unlike the negative T-cycle there is no continuity found in the $M(t)$ data measured during t_1 and t_3 for both ZFC and FC measurements in the positive T-cycle. This clearly suggests that positive T-cycling or temporary heating erases the memory and reinitializes the relaxation process in both ZFC and FC methods. Thus, no memory effect is observed when the temperature is restored back to 5 K.

The asymmetric response of magnetic relaxation with respect to both negative and positive T-cycles is typically observed for both SG and superparamagnetic systems. In SG systems, this behavior can be explained on the basis of the hierarchical model [81,82]. Similarly, for superparamagnetic systems, this behavior is very well explained by Tsoi *et al.* [24] and Bandyopadhyay *et al.* [26] in light of simple two-state superparamagnetic model [25]. Thus, the observed memory effects in ZFC and FC protocols for the negative T-cycle further justifies the superparamagnetic nature of the system under investigation.

IV. SUMMARY

We have successfully synthesized the polycrystalline sample of a modified cubic spinel compound LNMO. It is found to crystallize in a cubic structure with a noncentrosymmetric space group $P4_332$ and exhibits 1:3 cation order of Ni^{2+} and Mn^{4+} ions. Physical property measurements suggest semiconducting nature of the compound which exhibits a long-range ferrimagnetic ordering at $T_C \simeq 125$ K. The analysis of the neutron diffraction data reveals a collinear ferrimagnetic spin structure, with magnetic moments aligned along the [110] direction. The moments of each Ni^{2+} or Mn^{4+} sublattice are coupled ferromagnetically whereas the intersublattice interaction is antiferromagnetic. The compound is still frustrated due to competing AFM and FM interactions which is also the reason for the reduction of frustration ratio (f), despite a highly frustrated pyrochlore lattice geometry. The reduced ordered moment of Ni^{2+} or Mn^{4+} ions also indicates the presence of significant frustration.

The critical exponents obtained from the analysis of magnetization data near T_C via modified Arrott and Kouvel-Fisher plots fall in the category of 3D XY universality class. The reliability of these critical exponents and the value of T_C are further confirmed from the scaling of magnetization isotherms. A reversible MCE with a large value of ΔS_m and RCP has been observed over a wide temperature range across T_C which can be ascribed to the effect of magnetic frustration. Even the critical analysis of field dependent $|\Delta S_m^{peak}|$ and RCP curves produce exponents close to the ones obtained from the critical analysis of magnetization. The second-order nature of the phase transition has also been confirmed from the universal scaling of ΔS_m and the nature of $n(H, T)$ curve. Our results demonstrate that LNMO is a promising refrigerant material, where frustration associated with the competing exchange interactions drives MCE.

The magnetic relaxation below T_b follows stretched exponential function demonstrating that the system evolves through a number of metastable states. $\chi''(T)$ below T_C depicts multiple anomalies, likely due to the effect of magnetic frustration. The hump at $T = T_{f2}$ shows strong frequency dependency with unusual dynamics. It follows a Arrhenius behavior in the high-temperature regime ($T > 27$ K), suggesting superparamagnetic behavior and a power-law behavior in the low-temperature regime ($T < 27$ K), suggesting SG dynamics at low temperatures. However, the absence of ZFC memory effect below $T_b \simeq 120$ K rules out the possibility of SG transition and confirms the superparamagnetic behavior down to the lowest measured temperature. Indeed, the behavior of dc $\chi(T)$

measured in FC and ZFC conditions also seems to substantiate the superparamagnetic nature of the compound with blocking temperature $T_b \simeq 120$ K. Nevertheless, the critical slowing down behavior following a power law at low temperature and the absence of ZFC memory contradict each other and warrants further investigations.

[1] A. P. Ramiréz, Strongly geometrically frustrated magnets, Annu. Rev. Mater. Sci. **24**, 453 (1994); H. T. Diep *et al.*, *Frustrated Spin Systems* (World Scientific, Singapore, 2013).

[2] J. S. Gardner, M. J. P. Gingras, and J. E. Greedan, Magnetic pyrochlore oxides, Rev. Mod. Phys. **82**, 53 (2010).

[3] S.-H. Lee, H. Takagi, D. Louca, M. Matsuda, S. Ji, H. Ueda, Y. Ueda, T. Katsufuji, J.-H. Chung, S. Park, S.-W. Cheong, and C. Broholm, Frustrated magnetism and cooperative phase transitions in spinels, J. Phys. Soc. Jpn. **79**, 011004 (2010).

[4] C. Lacroix, A. Solontsov, and R. Ballou, Spin fluctuations in itinerant electron antiferromagnetism and anomalous properties of YScMn$_2$, Phys. Rev. B **54**, 15178 (1996).

[5] H. Ueda, A. Matsuo, K. Kindo, and K. Yoshimura, Spin frustration and field-induced transitions of modified pyrochlore fluorides ACr$_2$F$_6$ (A = Rb and Cs), J. Phys. Soc. Jpn. **83**, 014701 (2014).

[6] M. Brühwiler, S. M. Kazakov, N. D. Zhigadlo, J. Karpinski, and B. Batlogg, Superconductivity in the geometrically frustrated pyrochlore RbOs$_2$O$_6$, Phys. Rev. B **70**, 020503(R) (2004).

[7] D. Hirai, M. Bremholm, J. M. Allred, J. Krizan, L. M. Schoop, Q. Huang, J. Tao, and R. J. Cava, Spontaneous Formation of Zigzag Chains at the Metal-Insulator Transition in the CsW$_2$O$_6$, Phys. Rev. Lett. **110**, 166402 (2013).

[8] T. Fennell, M. J. Harris, S. Calder, M. Ruminy, M. Boehm, P. Steffens, M.-H. Lemée-Cailleau, O. Zaharko, A. Cervellino, and S. T. Bramwell, Multiple coulomb phase in the fluoride pyrochlore CsNiCrF$_6$, Nat. Phys. **15**, 60 (2019).

[9] J. M. Tarascon, E. Wang, F. K. Shokoohi, W. R. McKinnon, and S. Colson, The spinel phase of LiMn$_2$O$_4$ as a cathode in secondary lithium cells, J. Electrochem. Soc. **138**, 2859 (1991).

[10] I. Tomeno, Y. Kasuya, and Y. Tsunoda, Charge and spin ordering in LiMn$_2$O$_4$, Phys. Rev. B **64**, 094422 (2001); J. Sugiyama, T. Hioki, S. Noda, and M. Kontani, A ^{7}Li-NMR study on spinel LiMn$_2$O$_4$: the evidence of an antiferromagnetic transition at 40 K, J. Phys. Soc. Jpn. **66**, 1187 (1997).

[11] Y.-II Jang, F. C. Chou, and Y.-M. Chiang, Spin-glass behavior in LiMn$_2$O$_4$ spinel, Appl. Phys. Lett. **74**, 2504 (1999).

[12] X. K. Zhang, J. J. Yuan, Y. M. Xie, Y. Yu, F. G. Kuang, H. J. Yu, X. R. Zhu, and H. Shen, Phase coexistence and exchange-bias effect in LiMn$_2$O$_4$ nanorods, Phys. Rev. B **97**, 104405 (2018).

[13] J.-H. Kim, S.-T. Myung, C. S. Yoon, S. G. Kang, and Y.-K. Sun, Comparative study of LiNi$_{0.5}$Mn$_{1.5}$O$_{4-\delta}$ and LiNi$_{0.5}$Mn$_{1.5}$O$_4$ cathodes having two crystallographic structures: $Fd\bar{3}m$ and $P4_332$, Chem. Mater. **16**, 906 (2004).

[14] G. Blasse, Ferromagnetism and ferrimagnetism of oxygen spinels containing tetravalent manganese, J. Phys. Chem. Solids **27**, 383 (1966); K. Mukai and J. Sugiyama, An indicator to identify the Li[Ni$_{1/2}$Mn$_{3/2}$]O$_4$ ($P4_332$) : Dc-susceptibility measurements, J. Electrochem. Soc. **157**, A672 (2010); N. Amdouni, K. Zaghib, F. Gendron, A. Mauger, and C.M. Julien, Magnetic properties of LiNi$_{0.5}$Mn$_{1.5}$O$_4$ spinels prepared by wet chemical methods, J. Magn. Magn. Mater. **309**, 100 (2007).

[15] L. Cai, Z. Liu, K. An, and C. Liang, Unraveling structural evolution of LiNi$_{0.5}$Mn$_{1.5}$O$_4$ by in situ neutron diffraction, J. Mater. Chem. A **1**, 6908 (2013); E.-S. Lee and A. Manthiram, Influence of doping on the cation ordering and charge-discharge behavior of LiMn$_{1.5}$Ni$_{0.5-x}$$M_xO_4$ (M = Cr, Fe, Co, and Ga) spinels between 5.0 and 2.0 V, *ibid.* **1**, 3118 (2013).

[16] J. Rodríguez-Carvajal, Recent advances in magnetic structure determination by neutron powder diffraction, Physica B (Amsterdam) **192**, 55 (1993).

[17] W. Branford, M. A. Green, and D. A. Neumann, Structure and ferromagnetism in Mn^{4+} spinels: AM$_{0.5}$Mn$_{1.5}$O$_4$ (A = Li, Cu; M = Ni, Mg), Chem. Mater. **14**, 1649 (2002).

[18] M. Kunduraci and G. G. Amatucci, Synthesis and characterization of nanostructured 4.7 v Li$_x$Ni$_{0.5}$Mn$_{1.5}$O$_4$ spinels for high-power lithium-ion batteries, J. Electrochem. Soc. **153**, A1345 (2006); L. Wang, H. Li, X. Huang, and E. Baudrin, A comparative study of $Fd\bar{3}m$ and $P4_332$ "LiNi$_{0.5}$Mn$_{1.5}$O$_4$", Solid State Ion. **193**, 32 (2011).

[19] A. L. Patterson, The scherrer formula for x-ray particle size determination, Phys. Rev. **56**, 978 (1939).

[20] S. S. Islam, K. M. Ranjith, M. Baenitz, Y. Skourski, A. A. Tsirlin, and R. Nath, Frustration of square cupola in Sr(TiO)Cu$_4$(PO$_4$)$_4$, Phys. Rev. B **97**, 174432 (2018).

[21] R. Nath, V. O. Garlea, A. I. Goldman, and D. C. Johnston, Synthesis, structure, and properties of tetragonal Sr$_2$$M_3As_2O_2$ (M_3 = Mn$_3$, Mn$_2$Cu, and MnZn$_2$) compounds containing alternating CuO$_2$-type and FeAs-type layers, Phys. Rev. B **81**, 224513 (2010).

[22] P. Bag, P. R. Baral, and R. Nath, Cluster spin-glass behavior and memory effect in Cr$_{0.5}$Fe$_{0.5}$Ga, Phys. Rev. B **98**, 144436 (2018).

[23] P. Bag, K. Somesh, and R. Nath, A study of cluster spin-glass behavior at the critical composition Mn$_{0.73}$Fe$_{0.27}$NiGe, J. Magn. Magn. Mater. **497**, 165977 (2020).

[24] G. M. Tsoi, L. E. Wenger, U. Senaratne, R. J. Tackett, E. C. Buc, R. Naik, P. P. Vaishnava, and V. Naik, Memory effects in a superparamagnetic γ-Fe$_2$O$_3$ system, Phys. Rev. B **72**, 014445 (2005).

[25] M. Sasaki, P. E. Jönsson, H. Takayama, and H. Mamiya, Aging and memory effects in superparamagnets and superspin glasses, Phys. Rev. B **71**, 104405 (2005).

[26] M. Bandyopadhyay and S. Dattagupta, Memory in nanomagnetic systems: Superparamagnetism versus spin-glass behavior, Phys. Rev. B **74**, 214410 (2006).

[27] X. Chen, S. Bedanta, O. Petracic, W. Kleemann, S. Sahoo, S. Cardoso, and P. P. Freitas, Superparamagnetism versus superspin glass behavior in dilute magnetic nanoparticle systems, Phys. Rev. B **72**, 214436 (2005).

[28] C. Kittel, P. McEuen, and P. McEuen, *Introduction to Solid State Physics* (Wiley, New York, 1976), Vol. 8.

[29] Y. C. Sun, Z. W. Ouyang, J. F. Wang, Z. X. Wang, Z. C. Xia, and G. H. Rao, Breaking of 1D magnetism in a spin-1 chain antiferromagnet $Ni_2V_2O_7$: ESR and first-principles studies, Eur. Phys. J. Plus **131**, 343 (2016); J. Werner, W. Hergett, M. Gertig, J. Park, C. Koo, and R. Klingeler, Anisotropy-governed competition of magnetic phases in the honeycomb quantum magnet $Na_3Ni_2SbO_6$ studied by dilatometry and high-frequency ESR, Phys. Rev. B **95**, 214414 (2017); M. Y. Ruan, Z. W. Ouyang, S. S. Sheng, X. M. Shi, Y. M. Guo, J. J. Cheng, and Z. C. Xia, High-field magnetization and ESR studies of spin-chain compound Ca_3CoMnO_6, J. Magn. Magn. Mater. **344**, 55 (2013).

[30] C. Domb and A. R. Miedema, *Magnetic Transitions*, (Elsevier, Amsterdam, 1964), p. 296.

[31] A. P. Ramiréz *et al.*, *Handbook of Magnetic Materials* (Elsevier, Amsterdam, 2001), Vol. 13, p. 423.

[32] E. S. R. Gopal, *Specific Heats at Low Temperatures* (Springer, New York, 2012).

[33] J. O. Thomson and J. R. Thompson, Low-temperature excitations in spin glasses: evidence for a $T^{3/2}$ behaviour, J. Phys. F: Met. Phys. **11**, 247 (1981).

[34] D. C. Johnston, R. J. McQueeney, B. Lake, A. Honecker, M. E. Zhitomirsky, R. Nath, Y. Furukawa, V. P. Antropov, and Y. Singh, Magnetic exchange interactions in $BaMn_2As_2$: A case study of the J_1-J_2-J_c heisenberg model, Phys. Rev. B **84**, 094445 (2011).

[35] R. Nath, K. M. Ranjith, B. Roy, D. C. Johnston, Y. Furukawa, and A. A. Tsirlin, Magnetic transitions in the spin-$\frac{5}{2}$ frustrated magnet $BiMn_2PO_6$ and strong lattice softening in $BiMn_2PO_6$ and $BiZn_2PO_6$ below 200 K, Phys. Rev. B **90**, 024431 (2014).

[36] J. Kanamori, Superexchange interaction and symmetry properties of electron orbitals, J. Phys. Chem. Solids **10**, 87 (1959); J. B. Goodenough, Theory of the role of covalence in the perovskite-type manganites $LaM(II)MnO_3$, Phys. Rev. **100**, 564 (1955).

[37] Y. Shimakawa, Y. Kubo, N. Hamada, J. D. Jorgensen, Z. Hu, S. Short, M. Nohara, and H. Takagi, Crystal structure, magnetic and transport properties, and electronic band structure of $A_2Mn_2O_7$ pyrochlores (A = Y, In, Lu, and Tl), Phys. Rev. B **59**, 1249 (1999).

[38] K. Manna, A. K. Bera, M. Jain, S. Elizabeth, S. M. Yusuf, and P. S. Anil Kumar, Structural-modulation-driven spin canting and reentrant glassy magnetic phase in ferromagnetic Lu_2MnNiO_6, Phys. Rev. B **91**, 224420 (2015).

[39] K. M. Ranjith, R. Nath, M. Majumder, D. Kasinathan, M. Skoulatos, L. Keller, Y. Skourski, M. Baenitz, and A. A. Tsirlin, Commensurate and incommensurate magnetic order in spin-1 chains stacked on the triangular lattice in $Li_2NiW_2O_8$, Phys. Rev. B **94**, 014415 (2016); K. M. Ranjith, M. Majumder, M. Baenitz, A. A. Tsirlin, and R. Nath, Frustrated three-dimensional antiferromagnet $Li_2CuW_2O_8$: ^7Li NMR and the effect of nonmagnetic dilution, *ibid.* **92**, 024422 (2015).

[40] T. Moriya, Nuclear magnetic relaxation in antiferromagnetics, Prog. Theor. Phys. **16**, 23 (1956).

[41] H. E. Stanley, *Phase Transitions and Critical Phenomena* (Clarendon, Oxford, 1971).

[42] A. Arrott and J. E. Noakes, Approximate Equation of State for Nickel Near its Critical Temperature, Phys. Rev. Lett. **19**, 786 (1967).

[43] A. Arrott, Criterion for ferromagnetism from observations of magnetic isotherms, Phys. Rev. **108**, 1394 (1957).

[44] B. K. Banerjee, On a generalised approach to first and second order magnetic transitions, Phys. Lett. **12**, 16 (1964).

[45] J. S. Kouvel and M. E. Fisher, Detailed magnetic behavior of nickel near its curie point, Phys. Rev. **136**, A1626 (1964).

[46] S. N. Kaul, Static critical phenomena in ferromagnets with quenched disorder, J. Magn. Magn. Mater. **53**, 5 (1985).

[47] B. Widom, Equation of state in the neighborhood of the critical point, J. Chem. Phys. **43**, 3898 (1965).

[48] M. D. Lumsden, B. D. Gaulin, H. Dabkowska, and M. L. Plumer, Critical Phenomena of the Spin-Peierls Transition in $CuGeO_3$, Phys. Rev. Lett. **76**, 4919 (1996).

[49] R. Reisser, R. K. Kremer, and A. Simon, 3d-XY critical behavior of the layered metal-rich halides Gd_2IFe_2, Gd_2ICo_2 and Gd_2BrFe_2, Physica B (Amsterdam) **204**, 265 (1995).

[50] V. Franco, J. S. Blázquez, B. Ingale, and A. Conde, The magnetocaloric effect and magnetic refrigeration near room temperature: Materials and models, Annu. Rev. Mater. Res. **42**, 305 (2012).

[51] M. E. Zhitomirsky, Enhanced magnetocaloric effect in frustrated magnets, Phys. Rev. B **67**, 104421 (2003).

[52] A. M. Tishin and Y. I. Spichkin, *The Magnetocaloric Effect and Its Applications* (CRC Press, Boca Raton, FL, 2016).

[53] S. S. Sosin, L. A. Prozorova, A. I. Smirnov, A. I. Golov, I. B. Berkutov, O. A. Petrenko, G. Balakrishnan, and M. E. Zhitomirsky, Magnetocaloric effect in pyrochlore antiferromagnet $Gd_2Ti_2O_7$, Phys. Rev. B **71**, 094413 (2005); M. Das, S. Roy, N. Khan, and P. Mandal, Giant magnetocaloric effect in an exchange-frustrated $GdCrTiO_5$ antiferromagnet, *ibid.* **98**, 104420 (2018).

[54] T. Chakraborty, H. Nhalil, R. Yadav, A. A. Wagh, and S. Elizabeth, Magnetocaloric properties of R_2NiMnO_6R(=Pr, Nd, Tb, Ho and Y) double perovskite family, J. Magn. Magn. Mater. **428**, 59 (2017).

[55] X. Q. Zheng, J. Chen, J. Shen, Hu Zhang, Z. Y. Xu, W. W. Gao, J. F. Wu, F. X. Hu, J. R. Sun, and B. G. Shen, Large refrigerant capacity of RGa (R = Tb and Dy) compounds, J. Appl. Phys. **111**, 07A917 (2012).

[56] J. Y. Zhang, J. Luo, J. B. Li, J. K. Liang, Y. C. Wang, L. N. Ji, Y. H. Liu, and G. H. Rao, Magnetocaloric effect of $Gd(Co_{1-x}Mn_x)_2$ compounds, Solid State Commun. **143**, 541 (2007).

[57] E. Yuzuak, B. Emre, Y. Elerman, and A. Yucel, Giant magnetocaloric effect in $Tb_5Ge_{2-x}Si_{2-x}Mn_{2x}$, Chin. Phys. B **19**, 057501 (2010).

[58] M. Balli, D. Fruchart, and D. Gignoux, Effect of ni substitution on the magnetic and magnetocaloric properties of the $Dy(Co_{1-x}Ni_x)_2$ laves phase, J. Phys. D: Appl. Phys. **40**, 7601 (2007).

[59] V. Paul-Boncour and T. Mazet, Investigation of compounds for magnetocaloric applications: $YFe_2H_{4.2}$, $YFe_2D_{4.2}$, and $Y_{0.5}Tb_{0.5}Fe_2D_{4.2}$, J. Appl. Phys. **105**, 013914 (2009).

[60] V. Franco, J. S. Blázquez, and A. Conde, Field dependence of the magnetocaloric effect in materials with a second order phase transition: A master curve for the magnetic entropy change, Appl. Phys. Lett. **89**, 222512 (2006); V. Franco, C. F. Conde, J. S. Blázquez, A. Conde, P. Švec, D. Janičkovič, and L. F. Kiss,

A constant magnetocaloric response in FeMoCuB amorphous alloys with different Fe\B ratios, J. Appl. Phys. **101**, 093903 (2007).

[61] C. M. Bonilla, J. Herrero-Albillos, F. Bartolomé, L. M. García, M. Parra-Borderías, and V. Franco, Universal behavior for magnetic entropy change in magnetocaloric materials: An analysis on the nature of phase transitions, Phys. Rev. B **81**, 224424 (2010).

[62] V. Singh, P. Bag, R. Rawat, and R. Nath, Critical behavior and magnetocaloric effect across the magnetic transition in $Mn_{1+x}Fe_{4-x}Si_3$, Sci. Rep. **10**, 6981 (2020).

[63] J. Y. Law, V. Franco, L. M. Moreno-Ramírez, A. Conde, D. Y. Karpenkov, I. Radulov, K. P. Skokov, and O. Gutfleisch, A quantitative criterion for determining the order of magnetic phase transitions using the magnetocaloric effect, Nat. Commun. **9**, 2680 (2018).

[64] J. Dho, W. S. Kim, and N. H. Hur, Reentrant Spin Glass Behavior in Cr-Doped Perovskite Manganite, Phys. Rev. Lett. **89**, 027202 (2002).

[65] R. Mahendiran, Y. Bréard, M. Hervieu, B. Raveau, and P. Schiffer, Giant frequency dependence of dynamic freezing in nanocrystalline ferromagnetic $LaCo_{0.5}Mn_{0.5}O3$, Phys. Rev. B **68**, 104402 (2003).

[66] J. A. Mydosh, *Spin Glasses: An Experimental Introduction* (CRC Press, Boca Raton, FL, 2014).

[67] C. A. M. Mulder, A. J. van Duyneveldt, and J. A. Mydosh, Frequency and field dependence of the ac susceptibility of the AuMn spin-glass, Phys. Rev. B **25**, 515 (1982).

[68] K. Binder and A. P. Young, Spin glasses: Experimental facts, theoretical concepts, and open questions, Rev. Mod. Phys. **58**, 801 (1986).

[69] M. Suzuki, I. S. Suzuki, N. Wada, and M. S. Whittingham, Superparamagnetic behavior in a Ni vermiculite intercalation compound, Phys. Rev. B **64**, 104418 (2001).

[70] J. Kumar, S. N. Panja, D. John Mukkattukavil, A. Bhattacharyya, A. K. Nigam, and S. Nair, Reentrant superspin glass state and magnetization steps in the oxyborate Co_2AlBO_5, Phys. Rev. B **95**, 144409 (2017).

[71] J. Souletie and J. L. Tholence, Critical slowing down in spin glasses and other glasses: Fulcher versus power law, Phys. Rev. B **32**, 516 (1985).

[72] M. Viswanathan and P. S. Anil Kumar, Observation of reentrant spin glass behavior in $LaCo_{0.5}Ni_{0.5}O_3$, Phys. Rev. B **80**, 012410 (2009); N. Hanasaki, K. Watanabe, T. Ohtsuka, I. Kézsmárki, S. Iguchi, S. Miyasaka, and Y. Tokura, Nature of the Transition Between a Ferromagnetic Metal and a Spin-Glass Insulator in Pyrochlore Molybdates, Phys. Rev. Lett. **99**, 086401 (2007).

[73] J. A. Quilliam, S. Meng, C. G. A. Mugford, and J. B. Kycia, Evidence of Spin Glass Dynamics in Dilute $LiHo_xY_{1-x}F_4$, Phys. Rev. Lett. **101**, 187204 (2008).

[74] J. Kroder, K. Manna, D. Kriegner, A. S. Sukhanov, E. Liu, H. Borrmann, A. Hoser, J. Gooth, W. Schnelle, D. S. Inosov, G. H. Fecher, and C. Felser, Spin glass behavior in the disordered half-heusler compound IrMnGa, Phys. Rev. B **99**, 174410 (2019).

[75] F. Alvarez, A. Alegria, and J. Colmenero, Relationship between the time-domain kohlrausch-williams-watts and frequency-domain havriliak-negami relaxation functions, Phys. Rev. B **44**, 7306 (1991).

[76] D. De, A. Karmakar, M. K. Bhunia, A. Bhaumik, S. Majumdar, and S. Giri, Memory effects in superparamagnetic and nanocrystalline $Fe_{50}Ni_{50}$ alloy, J. Appl. Phys. **111**, 033919 (2012).

[77] D. X. Li, Y. Shiokawa, Y. Homma, A. Uesawa, A. Dönni, T. Suzuki, Y. Haga, E. Yamamoto, T. Honma, and Y. Ōnuki, Evidence for the formation of the spin-glass state in U_2PdSi_3, Phys. Rev. B **57**, 7434 (1998).

[78] B. Derrida, Random-energy model: An exactly solvable model of disordered systems, Phys. Rev. B **24**, 2613 (1981); J. P. Bouchaud, Weak ergodicity breaking and aging in disordered systems, J. Phys. I (France) **2**, 1705 (1992).

[79] D. S. Fisher and D. A. Huse, Nonequilibrium dynamics of spin glasses, Phys. Rev. B **38**, 373 (1988).

[80] A. Bajpai and A. Banerjee, Superparamagnetism in polycrystalline $Li_{0.5}Ni_{0.5}O$ samples: Low-field susceptibility measurements, Phys. Rev. B **62**, 8996 (2000); M. Bałanda, M. Rams, S. K. Nayak, Z. Tomkowicz, W. Haase, K. Tomala, and J. V. Yakhmi, Slow magnetic relaxations in the anisotropic heisenberg chain compound Mn(III) tetra(orthofluorophenyl)porphyrin-tetracyanoethylene, *ibid.* **74**, 224421 (2006).

[81] Y. Sun, M. B. Salamon, K. Garnier, and R. S. Averback, Memory Effects in an Interacting Magnetic Nanoparticle System, Phys. Rev. Lett. **91**, 167206 (2003).

[82] F. Lefloch, J. Hammann, M. Ocio, and E. Vincent, Can aging phenomena discriminate between the droplet model and a hierarchical description in spin glasses? Europhys. Lett. **18**, 647 (1992).